Timing of exhumation of meta-ophiolite units in the Western Alps: New tectonic implications from 40Ar/39Ar white mica ages from Piedmont Zone (Susa Valley)

LITHOS

Timing of exhumation of meta-ophiolite units in the Western Alps: new tectonic implications from 40Ar/39Ar white mica ages from Piedmont Zone (Susa Valley)

--Manuscript Draft--

Manuscript Number:	
Article Type:	Regular Article
Keywords:	40Ar/39Ar; exhumation; meta-ophiolites; Piedmont Zone; Western Alps
Corresponding Author:	Stefano Ghignone University of Turin: Universita degli Studi di Torino ITALY
First Author:	Stefano Ghignone
Order of Authors:	Stefano Ghignone
	Masafumi Sudo
	Gianni Balestro
	Alessandro Borghi
	Marco Gattiglio
	Silvio Ferrero
	Valby van Schijndel
Abstract:	Abstract A multidisciplinary approach to the study of collisional orogenic belts can improve our knowledge of their geodynamic evolution and may suggest new tectonic models, especially for (U)HP rocks inside the accretionary wedge. In the Western Alps, wherein nappes of different origin are stacked, having recorded different metamorphic peaks at different stages of the orogenic evolution. This study focuses on the External (EPZ) and Internal (IPZ) ophiolitic units of the Piedmont Zone (Susa Valley, Western Alps), which were deformed throughout four tectonometamorphic phases (D1 to D4), developing different foliations and cleavages (S1 to S4) at different metamorphic conditions. The IPZ and EPZ are separated by a shear zone (i.e. the Susa Shear Zone) during which a related mylonitic foliation (SM) developed. S1 developed at high pressure conditions (Epidote-eclogite vs. Lawsonite-blueschist facies conditions for IPZ and EPZ, respectively), as suggested by the composition of white mica (i.e. phengite), whereas S2 developed at low pressure conditions (Epidote-greenschist facies conditions in both IPZ and EPZ) and is defined by muscovite. White mica defining the SM mylonitic foliation (T1) is mostly defined by phengite, while the T2-related disjunctive cleavage is defined by fine-grained muscovite. The relative chronology inferred from meso- and micro-structural observations suggests that T1 was near-coeval respect to the D2, while T2 developed during D4. A new set of radiometric ages of the main metamorphic foliations were obtained by in situ Ar/Ar dating on white mica. Different generations of white mica defining S1 and S2 foliations in both the IPZ and EPZ and SM in the SSZ, were dated and two main groups of ages were obtained. In both IPZ and EPZ, S1 foliation developed at ~46-41 Ma, while S2 foliation developed at ~40-36 Ma and was nearly coeval with the SM mylonitic foliation (~39-36 Ma). Comparison between structural, petrological and geochronological data allows to define time of coupling of the different units and consequently to infer new tectonic implications for the exhumation of meta-ophiolites of the Piedmont Zone within axial sector of the Western Alps.
Suggested Reviewers:	Samuel Angiboust angiboust@ipgp.fr
	Paola Tartarotti paola.tartarotti@unimi.it
	Tetsumaru Itaya

	tetsumaru.itaya@gmail.com
Opposed Reviewers:	

Timing of exhumation of meta-ophiolite units in the Western Alps: new tectonic implications from $^{40}Ar/^{39}Ar$ white mica ages from Piedmont Zone (Susa Valley)

Ghignone, S.[1]*, Sudo, M.[2], Balestro, G.[1], Borghi, A.[1], Gattiglio, M.[1], Ferrero, S.[2,3], van Schijndel, V.[2]

1 Earth Sciences Department, University of Turin, Via Valperga Caluso 35, 10125 Torino, Italy,

2 Institut für Geowissenschaften, Universität Potsdam, Karl-Liebknecht-Str. 24-25, 14476 Potsdam, Deutschland,

3 Museum für Naturkunde (MfN), Leibniz-Institut für Evolutions- und Biodiversitätsforschung, Chaussee-Str. 111, 10115 Berlin, Deutschland.

* Corresponding author: s.ghignone@unito.it

Stefano Ghignone

Dipartimento di Scienze della Terra

Università di Torino

Via Valperga Caluso, 35

10125 – Torino (Italy)

Email: s.ghignone@unito.it

Phone: +39-011 670 51 26

Abstract

A multidisciplinary approach to the study of collisional orogenic belts can improve our knowledge of their geodynamic evolution and may suggest new tectonic models, especially for (U)HP rocks inside the accretionary wedge. In the Western Alps, wherein nappes of different origin are stacked, having recorded different metamorphic peaks at different stages of the orogenic evolution. This study focuses on the External (EPZ) and Internal (IPZ) ophiolitic units of the Piedmont Zone (Susa Valley, Western Alps), which were deformed throughout four tectonometamorphic phases (D1 to D4), developing different foliations and cleavages (S1 to S4) at different metamorphic conditions. The IPZ and EPZ are separated by a shear zone (i.e. the Susa Shear Zone) during which a related mylonitic foliation (SM) developed. S1 developed at high pressure conditions (Epidote-eclogite vs. Lawsonite-blueschist facies conditions for IPZ and EPZ, respectively), as suggested by the composition of white mica (i.e. phengite), whereas S2 developed at low pressure conditions (Epidote-greenschist facies conditions in both IPZ and EPZ) and is defined by muscovite. White mica defining the SM mylonitic foliation (T1) is mostly defined by phengite, while the T2-related disjunctive cleavage is defined by fine-grained muscovite. The relative chronology inferred from meso- and micro-structural observations suggests that T1 was near-coeval respect to the D2, while T2 developed during D4.

A new set of radiometric ages of the main metamorphic foliations were obtained by in situ Ar/Ar dating on white mica. Different generations of white mica defining S1 and S2 foliations in both the IPZ and EPZ and SM in the SSZ, were dated and two main groups of ages were obtained. In both IPZ and EPZ, S1 foliation developed at ~46-41 Ma, while S2 foliation developed at ~40-36 Ma and was nearly coeval with the SM mylonitic foliation (~39-36 Ma).

Comparison between structural, petrological and geochronological data allows to define time of coupling of the different units and consequently to infer new tectonic implications for the exhumation of meta-ophiolites of the Piedmont Zone within axial sector of the Western Alps.

Highlights

- Middle Eocene high pressure metamorphic events in meta-ophiolite of the Piedmont Zone ((NW Italy) .
- Late Eocene coupling between Internal and External Piedmont Zone along the Susa Shear Zone
- Different exhumation rates and apparent top-to-East shearing event along the Susa Shear Zone

Timing of exhumation of meta-ophiolite units in the Western Alps: new tectonic implications from $^{40}Ar/^{39}Ar$ white mica ages from Piedmont Zone (Susa Valley)

Ghignone, S.[1]*, Sudo, M.[2], Balestro, G.[1], Borghi, A.[1], Gattiglio, M.[1], Ferrero, S.[2,3], van Schijndel, V.[2]

1 Earth Sciences Department, University of Turin, Via Valperga Caluso 35, 10125 Torino, Italy,

2 Institut für Geowissenschaften, Universität Potsdam, Karl-Liebknecht-Str. 24-25, 14476 Potsdam, Deutschland,

3 Museum für Naturkunde (MfN), Leibniz-Institut für Evolutions- und Biodiversitätsforschung, Chaussee-Str. 111, 10115 Berlin, Deutschland.

* Corresponding author: s.ghignone@unito.it

Abstract

A multidisciplinary approach to the study of collisional orogenic belts can improve our knowledge of their geodynamic evolution and may suggest new tectonic models, especially for (U)HP rocks inside the accretionary wedge. In the Western Alps, wherein nappes of different origin are stacked, having recorded different metamorphic peaks at different stages of the orogenic evolution. This study focuses on the External (EPZ) and Internal (IPZ) ophiolitic units of the Piedmont Zone (Susa Valley, Western Alps), which were deformed throughout four tectonometamorphic phases (D1 to D4), developing different foliations and cleavages (S1 to S4) at different metamorphic conditions. The IPZ and EPZ are separated by a shear zone (i.e. the Susa Shear Zone) during which a related mylonitic foliation (SM) developed. S1 developed at high pressure conditions (Epidote-eclogite vs. Lawsonite-blueschist facies conditions for IPZ and EPZ, respectively), as suggested by the composition of white mica (i.e. phengite), whereas S2 developed at low pressure conditions (Epidote-greenschist facies conditions in both IPZ and EPZ) and is defined by muscovite. White mica defining the SM mylonitic foliation (T1) is mostly defined by phengite, while the T2-related disjunctive cleavage is defined by fine-grained muscovite. The relative chronology inferred from meso- and micro-structural observations suggests that T1 was near-coeval respect to the D2, while T2 developed during D4.

A new set of radiometric ages of the main metamorphic foliations were obtained by in situ Ar/Ar dating on white mica. Different generations of white mica defining S1 and S2 foliations in both the IPZ and EPZ and SM in the SSZ, were dated and two main groups of ages were obtained. In both IPZ and EPZ, S1 foliation developed at ~46-41 Ma, while S2 foliation developed at ~40-36 Ma and was nearly coeval with the SM mylonitic foliation (~39-36 Ma).

Comparison between structural, petrological and geochronological data allows to define time of coupling of the different units and consequently to infer new tectonic implications for the exhumation of meta-ophiolites of the Piedmont Zone within axial sector of the Western Alps.

Keywords: $^{40}Ar/^{39}Ar$, exhumation, meta-ophiolites, Piedmont Zone, Western Alps

1. Introduction

Unravelling deformation history recorded in mountain ranges provide important information for reconstructing their tectono-metamorphic evolution. The geochronological approach, combined with fieldwork and detailed petrographic studies, provide constraints in absolute time for the geodynamic evolution of orogens. The most interesting results expected from this kind of studies come from shear zones, which are key-sectors for studying the stacking of rock volumes belonging to different geological units. In particular, the evolution of stacked nappes and their timing of deformation in orogenic chains can be inferred by comparing data collected along shear zones with those coming from their footwall and hanging wall blocks.

In the Western Alps, studies giving geochronological constraints are mainly focused on dating subduction-related HP metamorphism (see e.g., Rosenbaum and Lister, 2005, and Weber et al., 2015), whereas other works mainly aimed to constrain the exhumation history of tectonic units and related deformation phases (see e.g., Reddy et al., 2003, and Angiboust & Glodny, 2020).

In situ $^{40}Ar/^{39}Ar$ ultraviolet (UV) laser-ablation spot analyses is one of the most used methods for giving absolute time constraints and, in particular, data obtained from minerals oriented along metamorphic foliations provide ages of deformation (see e.g. Itaya et al., 2018; Wiederkehr et al., 2009; Villa et al., 2014 and reference therein).

Data from *in situ* $^{40}Ar/^{39}Ar$ UV laser-ablation spot analyses on white mica allow us to constrain the whole exhumation history of meta-ophiolitic units occurring along the Susa Valley section and within the Western Alpine axial sector.

This paper deals with metamorphic and deformation ages from Western Alpine meta-ophiolite units, exposed in the Susa Valley. The meta-ophiolite units are currently missing any geochronological constraints. *In situ* $^{40}Ar/^{39}Ar$ UV laser-ablation spot analyses is one of the most used methods for giving absolute time constraints and, in particular, data obtained from minerals oriented along metamorphic foliations provide ages of deformation (see e.g. Itaya et al., 2018; Wiederkehr et al., 2009; Villa et al., 2014 and reference therein).

We present new $^{40}Ar/^{39}Ar$ geochronological data on white mica obtained from well-constrained microstructural sites (i.e. superimposed foliations and related metamorphic imprints; see Ghignone et al., 2020a, 2020b). By taking into account ages of both P-T peaks and metamorphic re-equilibration, and of related deformation phases, it is possible to place new constraints on the timing of the whole exhumation history of meta-ophiolitic units occurring along the Susa Valley section and within the Western Alpine axial sector.

These new data are compared with published ages from other Western Alpine meta-ophiolite units (e.g., Cliff et al., 1998; Dal Piaz et al., 2001; Agard et al., 2002; Rubatto and Hermann, 2003; Dragovic et al., 2020) in order to discuss the timing of different tectono-metamorphic events along the belt and provide geodynamic interpretations on the exhumation history.

2. Geological setting

2.1 Geology of the Alpine belt

The Western Alps result from the convergence between the European lower plate and Adria upper plate after the closure of the interposed Jurassic Ligurian-Piedmont Ocean, followed by (i) Late Cretaceous to Middle Eocene subduction, (ii) Late Eocene to Early Oligocene continental collision and (iii) Late Oligocene to Neogene extensional tectonics (see e.g. Dal Piaz et al., 2003; Rosenbaum & Lister, 2005; Handy et al., 2010; Schmidt et al., 2017, and references therein). The Western Alpine axial sector corresponds to an exhumed fossil subduction-complex, which was overthrusted on the European foreland (see e.g. Ricou & Siddans, 1986; Coward & Dietrich 1989; Polino et al., 1990).

Remnants of the Ligurian-Piedmont Ocean (i.e., the Piedmont Zone; see e.g., Ernst & Dal Piaz, 1978; Lemoine & Tricart 1986; Vissers et al., 2013; Balestro et al., 2019) are now stacked in the Alpine wedge and they are generally divided into an Internal Piedmont Zone (IPZ) and an External Piedmont Zone (EPZ), which corresponds to the Zermatt-Saas-like and Combin-like units of Bearth (1967), respectively.

The IPZ consists of meta-ophiolites with a thin metasedimentary cover, (see e.g., Lombardo and Pognante, 1982; Tartarotti et al., 2017; 2019; Balestro et al., 2018; De Togni et al., 2021, and reference therein), and is mainly made up of serpentinite hosting Middle to Late Jurassic metagabbro bodies and overlain by mafic/ultramafic metabreccia and metabasalt lavas (Lombardo et al., 2002; Manatchal and Muntener, 2009; Festa et al., 2015). IPZ reached P-T peak under eclogite-facies conditions, followed by a pervasive greenschist facies overprint (see e.g., Bucher et al., 2005; Reddy et al., 1999 and references therein). P-T peak conditions in the range of ~520–600 °C and ~2.2–3.0 GPa were proposed for the Zermatt-Saas meta-ophiolites (Angiboust et al., 2009; Bucher et al., 2005) and similar conditions (i.e. of roughly 2.5 GPa and 550°C) were proposed for the Monviso meta-ophiolite Complex (Angiboust et al., 2012; Balestro et al., 2014; Groppo & Castelli, 2010, Agard, 2021).

EPZ consists of meta-sedimentary oceanic successions wherein meta-ophiolite bodies are embedded. Meta-ophiolite bodies are made up of serpentinite, metagabbro, mafic/ultramafic metabreccia and metabasalt (Tricart and Lemoine, 1991), whereas metasediments correspond to Middle Jurassic-Late Jurassic radiolarian metachert, marble and Cretaceous calcschist (Lemoine and Tricart, 1986; Cordey et al., 2012; Lagabrielle et al., 2015). The EPZ was metamorphosed under blueschist facies conditions and re-equilibrated under greenschist conditions (Agard et al., 2001; Schwartz et al., 2013 and references therein), and it reached different P-T conditions along the Western Alpine belt (e.g., 1.2–1.5 GPa and 425–500 °C for the Combin Unit; Cartwright & Barnicoat 2002; Negro et al., 2013, 1.1–1.4 GPa and 330–350 °C, 1.5-2.0 GPa and 370-450°C for the upper and middle Queyras Units, Agard et al. 2021, and Michard et al., 2004).

The eclogitic peak of the IPZ along the Alpine belt was dated between 50 and 43 Ma depending on the lithology and the dating technique, while the greenschist-facies re-equilibration ranges between 43 and 32 Ma (Agard et al., 2002; Agard, 2021; Amato et al., 1999; Bowtell et al., 1994; Cliff et al., 1998; Duchêne et al., 1997; Monié and Philippot, 1989; Rubatto & Hermann, 2003; Rubatto et al., 1998; Angiboust & Glodny, 2020; Dragovic et al., 2020). The age of peak-P in EPZ is slightly younger, ranging between 57 and 38 Ma, while

the greenschist-facies re-equilibration encompasses values between 39 and 35 Ma (Dal Piaz et al, 2001; Agard et al., 2002; Reddy et al., 1999; Rosenbaum & Lister, 2005; Weber et al., 2015). UHP conditions for the Lago di Cignana Unit of the Zermatt Zone (P>3.2 GPa; T = 590-605°C, Groppo et al., 2009) were dated at ~ 48 – 40 Ma (Skora et al., 2015; Dal Piaz et al., 2001; Rubatto et al., 1998; Amato et al., 1999; Gouzu et al., 2016). Recently, Angiboust & Glodny (2020) dated the age of shearing (Rb-Sr multi-mineral method) between IPZ and EPZ at 38-35 Ma, which is mostly coherent with other shearing ages previously calculated along the Western Alpine belt in the same structural position (e.g. 39-37 Ma, Reddy et al., 1999).

2.2 Geology of the study area

The study area (**Figure 1b**) is located in the Susa Valley, wherein IPZ is juxtaposed to the northern sector of the Dora Maira Massif (DM), a slab of the paleo-european thinned margin, and is overlain by the External Piedmont Zone (EPZ). These units were deformed throughout four regional deformation phases (D1 to D4): three common phases (D2 to D3) and an early HP phase (D1) that developed in eclogite-facies and blueschist-facies conditions in IPZ and EPZ, respectively. Each phase developed a different foliation or cleavage (S1 to S4; Gasco et al., 2011; Ghignone et al., 2020a, Ghignone et al., 2020b). In the study area, the DM and the overlying IPZ were folded together during early exhumation-related deformation phase (D2, Gasco et al. 2011) and are both separated from the EPZ through the Susa Shear Zone (SSZ; Ghignone & Gattiglio, 2013; Ghignone et al., 2020a). Along the SSZ, two different events of shearing occur (T1 and T2) (Ghignone et al., 2020b). T1 shearing is defined by a mylonitic foliation (SM) along which Top-to-E kinematics occur, while T2 is defined by a disjunctive cleavage along with Top-to-W kinematics (Ghignone et al., 2020a, Ghignone et al., 2020b).

In the Susa Valley, the IPZ consists of serpentinized metaperidotite, metagabbro and metabasite (Nicolas, 1966; Pognante, 1979; Pognante, 1980; Leardi & Rossetti, 1985; Balestro et al., 2009), and of a metasedimentary cover consisting of minor Mn-rich quartzite, impure marble and micaschist, and widespread calcschist. In this sector, recent estimations on IPZ (Ghignone et al., 2020c) allowed to identify two HP peaks (peak-P at P = 2.5-2.9 GPa, T = 460-510°C and peak-T at P = 2.1-2.5 GPa, T = 500-530°C) and a LP decompressional evolution, consisting of a strong greenschist facies re-equilibration and a near-isobaric late heating, at the boundary between greenschist and amphibolite facies conditions. Peak-T corresponds to the

development of the D1 deformation phase (characterized by S1 axial plane foliation), while greenschist facies re-equilibration corresponds to the D2 deformation phase (characterized by the development of the S2 regional foliation), as reported by Ghignone et al. (2020b; 2020c).

The underlying DM was metamorphosed under eclogite-facies P-T peak conditions (i.e. P = 1.9 GPa and T = 510°C; Gasco et al., 2011) and subsequently re-equilibrated under greenschist-to-amphibolite facies conditions (Gasco et al. 2011).

EPZ consists of a thick calcschists meta-sedimentary cover with bodies of metabasalt and serpentinite, and with interlayered paragneiss, quarzite and micaschist.

The metamorphic evolution of the EPZ was characterized by a HP peak developed in blueschist-facies conditons (P = 1.2-1.3 GPa, T = 350°C) and a LP re-equilibration in greenschist conditions Agard et al. (2001). These two metamorphic events likely correspond to the D1 (with the development of S1 axial plane foliation) and D2 (characterized by the development of the S2 regional foliation) deformation phases, respectively.

3. Petrography and microstructures

Six samples of metasediments (i.e. calcschist and micaschist) were selected from the study area for geochronological investigations. All sampled metasediments are white mica-rich and come from the lower IPZ (VS17, VS14), the upper EPZ (VS74, VS19) and the interposed SSZ (VS4, VS15). Locations of the collected samples are shown in **Figure 1b** (GPS coordinates in **Table 1**).

The samples collected in the SSZ contain pre-shearing structural relics. In particular, before mylonitization processes, VS15 and VS4 samples pertained to the IPZ and EPZ, respectively.

Main pervasive foliations (i.e. S1 and SM) and several relics of previous foliation (i.e. S1) occur in each sample. S1 and S2 foliations, locally, appear parallel each other, due to re-orientation during D2 stage. Analysed white mica crystals were distinguished based on their (i) microstructural position and (ii) composition. The latter have been detected by electronic microprobe (SEM-EDS), and were referred to a specific foliation (S1, S2 and SM) based on meso- and micro-scale observations. Mineral abbreviations in the text, figures and tables are from Whitney and Evans (2010).

3.1 IPZ Samples

VS17 sample is a garnet-bearing micaschist and contains mostly white mica, quartz, garnet, chlorite and minor chloritoid, tourmaline, biotite, plagioclase, with accessory rutile, titanite, zircon and apatite. The rock texture is characterized by mm-sized lens-shaped white mica aggregates, locally intergrowth with chlorite, which transitionally pass to sub-cm-sized stripes of quartz. White mica is dominant in the sample, wrapping mm-sized garnet, and it is partly re-equilibrated by chlorite and biotite (**Figure 2a**).

The main foliation (S2) is defined by the shape-preferred orientation of white mica aggregates. Kinematic indicators along the S2 at the microscale are represented by asymmetrical recrystallization tails of micas, asymmetrical strain shadows around garnet porphyroclasts and mica fishes, which show a Top-to-W sense of shear (as reported by Ghignone et al., 2020a). Some evidences of dynamic deformation occur in quartz domains, such as grain boundary migration and subgrain rotation (GBM and SGR; see Passchier & Trouw, 2005).

VS14 sample is a calcschist composed by calcite, white mica, quartz, chlorite and minor biotite and titanite. The texture is defined by a transition between calcite- and quartz-rich domains and phyllosilicates-rich domains, consisting of white mica, chlorite and biotite, where deformation is concentrated. Single flakes of white mica are scattered inside calcite- and quartz-rich layers. The main foliation present in the sample (S1) is defined by the preferred orientation of white mica and other phyllosilicates. Moreover, in the sample, are also present some kinematic indicators (i.e. S-C structure, mica fishes, mantled porphyroclasts), showing Top-to-E sense of shear, referred to T1-shearing event, which crosscuts and partly re-orient S1 foliation (**Figure 2b**).

3.2 SSZ Samples

VS15 is a mylonitic Grt-Cld-bearing micaschist, mainly composed of white mica, quartz, chloritoid, garnet, chlorite, graphite and minor biotite, plagioclase, tourmaline, apatite, rutile and titanite. The well-developed mylonitic foliation (SM) is the dominant structural element in the sample, which wraps cm- to mm-sized micro-lithons, which contain rootless D2-fold hinges (**Figure 2c**), defined by the older foliation (S1). The rock texture is characterized by a cm-scale layering, defined by discrete transition between quartz-rich and phyllosilicates-rich layers, strongly deformed by mylonitic foliation. Several kinematic indicators are present, mostly C-planes (S-C structures), δ- and σ-type mantled porphyroclasts, mica fishes and minor domino structure, showing Top-to-E sense of shear, related to T1-shearing event.

VS4 sample is a mylonitic calcschist, constituted by calcite and white mica, with minor quartz, chlorite, biotite and graphite. The rock is banded, alternating carbonate and quartz layers to phyllosilicates-rich ones. Some white mica flakes are moreover present in carbonate-quartz rich layers. The texture is defined by pervasive foliation (S1) defined by the preferred oriented white mica crystals, almost parallel to the compositional banding. A spaced mylonitic foliation (SM) is also present in the sample, which wrap several micro-lithons containing differently oriented older foliation (S1). Mm- to sub-mm scale kinematic indicators are present in the sample, such as S-C structures, mostly showing Top-to-E sense of shear. Locally, S1 and SM foliations are deformed in microfolds (i.e. CCC, compressional crenulation cleavage), related to D3 deformation phase.

The deformation is mostly concentrated in the weaker phyllosilicate-rich layers, although evidences of dynamic deformation occur also in the stiffer carbonate-quartz layers, such as polysynthetic twinning in calcite and SGR in quartz (**Figure 2d**).

In this sample are also present some later C-planes, mm- to cm-spaced, defining a disjunctive cleavage, constituted by very fine-grained white mica, showing Top-to-W sense of shear (referred to T2 shearing event).

3.3 EPZ Samples

VS74 is a fine-grained micaschist, composed of white mica, chlorite, quartz, albite, biotite and titanite. The rock texture is characterized by a weak layering defined by alternating mm-sized quartz-rich and phyllosilicates-rich layers. The rock sample is characterized by a pervasive main S2 foliation, defined by very fine-grained and irregularly shaped aggregates of white mica and minor chlorite, which locally crosscuts and re-orient the layering. The texture is strongly deformed by D2 micro-folds (**Figure 2e**), which re-orient S1 older foliation almost parallel to the banding. Some kinematic indicators occur along the S2 foliation, such as fine-grained mantled porphyroclasts, showing Top-to-W sense of shear (D2-related).

VS19 is a foliated calcschist, composed of white mica, calcite, quartz and minor chlorite, biotite. The texture is defined by an mm-spaced layering between calcite-rich domains and phyllosilicates-rich domains, where deformation is concentrated (**Figure 2f**). Single flakes of white mica are scattered in the quartz-rich domains. A strongly pervasive foliation (SM) is the dominant structural element in the sample, defined by preferred orientation of white mica and other phyllosilicates. The foliation is pervasive and sub-mm spaced, wrapping several porphyroclasts of white mica, which contain differently oriented S1 relics.

4. Mineral chemistry

The compositional variation of white mica (Si content) defining different foliation generations were investigated at the electron microprobe considering the microstructural position and the relative timing of growth.

Compositional data point analyses were collected using a JEOL IT300LV Scanning Electron Microscope at the Department of Earth Sciences, University of Torino. The instrument is equipped with an energy dispersive spectrometry (EDS) INCA Energy 200 system and an SDD X-Act3 detector (Oxford Instruments). Used working conditions were E = 15kV, I probe = 5nA, EDS process time = 1 micro-sec, 10^5 cnts/sec, live time = 30 sec. White mica analyses were recalculated as atoms per formula unit (a.p.f.u.) on the basis of 11 oxygens, using Minsort software (Petrakakis & Dietrich, 1995). Selected analyses of the different foliation-related white mica are given in **Table S1** (supplementary material).

In the studied samples white mica show a strong zonation along the muscovite-celadonite join (**Figure 3**). High celadonite contents are widely considered as a marker of high-pressure low-temperature metamorphic conditions, while muscovite rims are inferred as a decompression-related feature (e.g. Massonne and Schreyer, 1987). In **Figure 3** are reported the compositional variations for the recognized foliation (S1, S2 and SM) in each sample. Same-named foliations, in both IPZ and EPZ, present slightly different compositions, due to the different P-T conditions of growth, especially for the S1.

In IPZ samples, S1 foliation is defined by phengite (black diamonds in **Figure 3**), showing values of Si between 3.41 and 3.71 a.p.f.u., with similar values in micaschist samples (VS17 and VS15), while, in sample VS14, Si content on S1-related phengite is more concentrated in a restricted field, ranging between 3.47 and 3.51 a.p.f.u.. This variation is probably due to the different lithology (calcschist), which include a slight variation in the bulk composition of the rock. In VS15 and VS14 samples, S1-related white mica show Al and Si values laying above the muscovite-celadonite join, with slightly higher Al/Si ratio.

S2-related white mica is defined by muscovite (red triangles in **Figure 3**), showing values of Si between 3.09 and 3.38 a.p.f.u.. In VS17 sample, S2-related muscovite are concentrated in a restricted field, between 3.20 and 3.30 a.p.f.u., while in VS14 and VS15 samples the chemical variation is wider, ranging between 3.15 and 3.38 a.p.f.u. (VS14) and 3.09 and 3.25 a.p.f.u. (VS15).

In EPZ samples, S1-related white mica also resulted phengite (black diamonds in **Figure 3**), showing values of Si between 3.65 and 3.30 a.p.f.u.. The zoning is similar in samples VS74 and VS19, wherein the wide dispersion show similar values (3.60 – 3.35 a.p.f.u.). S1-related phengite in sample VS4 show a minor zoning, with values concentrated between 3.30 and 3.42 a.p.f.u..

S2-related white mica resulted muscovite (red triangles in **Figure 3**), showing values of Si between 3.05 and 3.31 a.p.f.u.. In all the three EPZ samples, the distribution is very similar and show the same zoning, and the values plot on the muscovite-celadonite join.

SM-related white mica present high Si content (phengite, green triangles in **Figure 3**) and show similar composition in all the samples, where it is present (3.59 – 3.31 a.p.f.u.). The relationships with the S1-related phengite vary from sample to sample, showing similar compositions (VS15, VS19), lower Si content (VS17, VS14) and higher Si content (VS4), respectively. In sample VS74 SM-related phengite is not present.

5. *In situ* $^{40}Ar/^{39}Ar$ dating

Foliations recognized at the meso- and micro-scales (S1, S2 and SM) were dated applying *in situ* $^{40}Ar/^{39}Ar$ UV laser ablation spot analyses (see e.g., Maluski & Monié, 1988; Kelley et al., 1994), performed at the Potsdam University. The procedure of sample preparation and the operating conditions are similar to those reported by Wiederkehr et al. (2009), Wilke et al. (2010) and Halama et al. (2014).

As stated before, the accurate microstructural and compositional control on white mica crystals (**Figure 4**) allowed accurate *in situ* spot analyses along different foliation generations. Some of the single ages are reported in **Figure 5, 6, 7** in correspondence of measurements sites, allowing identification of the relationships between apparent ages (i.e., ages obtained in each site, punctual analyses) and the location of the dated domains in the microstructural context. The results of the *in situ* laser probe experiments are listed in **Table 2** (full detailed results are reported in **Table S2**). All isotopic ages and calculated weighted averages are quoted with their 2σ uncertainties; error on single ages include the uncertainty in the J value.

5.1 $^{40}Ar/^{39}Ar$ dating procedure

5.1.1 Sample preparation

277 Rock sections of almost 500 µm thickness and 12x12 mm in size have been cut out from double-polished thick
278 sections. Referring to thin section for petrographic description and mineral chemistry, the samples for dating
279 have been prepared from the opposite cut-out side of the hand specimen. Details from optical microscope
280 photographs (**Figure 2**), microprobe quantitative maps (**Figure 4**) of some polished surfaces and BSE imaging
281 (**Figure 5, 6, 7**) provided (*i*) an accurate pattern of the distribution of K-bearing white micas and (*ii*) the control
282 on the chemical zoning and the intergrowth of different phases (e.g., chlorite intergrowing with muscovite).
283 All these information were fundamental for selecting the most suitable places for performing the laser ablation-
284 spot $^{40}Ar/^{39}Ar$ isotope analysis.

285 **5.1.2 Neutron activation**

286 Neutron activation of polished sections was performed at CLICIT (Cadmium-Lined In-Core Irradiation Tube)
287 facility in the nuclear reactor OSTR (Oregon State TRIGA Reactor), Oregon State University, USA. The six
288 samples were wrapped in Al foil and subsequently loaded into a sample container (22.7 mm in diameter and
289 101.5 mm in height) made of 99.999% pure Al. All samples were irradiated for 4 hours with the fast neutrons
290 of the flux of $2.47x10^{13}$ n/cm^2/s for inducing reactions of ^{39}K (n, p) ^{39}Ar in the samples. The $^{40}Ar/^{39}Ar$ ages
291 were obtained as relative ages against the neutron flux (or J value) monitoring mineral standard, which was
292 irradiated together with unknown samples. The used age standard was Fish Canyon Tuff sanidine, FC3, which
293 was prepared at the Geological Survey of Japan and its age was determined as 27.5 Ma (Uto et al., 1997;
294 Ishizuka, 1998). This age is consistent with that obtained by Lanphere & Baadsgaard (2001). Additionally,
295 crystals of K_2SO_4 and CaF_2 were also irradiated for correcting the interference of Ar isotopes produced by the
296 reactions of K or Ca in the samples during neutron irradiation. After the irradiation the samples were stored
297 for a few weeks at OSTR to cool down their radioactivities. Finally, argon isotope analyses were performed at
298 the $^{40}Ar/^{39}Ar$ geochronology laboratory in the University of Potsdam.

299 **5.1.3 Ar isotope analysis**

300 The $^{40}Ar/^{39}Ar$ dating system consists of: (*i*) a Micromass 5400 high sensitivity–low background sector-type
301 noble gas mass spectrometer, (*ii*) a New Wave Research DualWave laser ablation system comprising a 50W
302 CO_2 continuous laser (10.6 µm wavelength) and a 6 mJ UV pulsed laser (266 nm wavelength, frequency
303 quadrupled), and (*iii*) an ultrahigh vacuum, all-metal purification line which includes Zr-Al SAES alloy getters
304 and a cold trap. The cold trap is a stainless-steel finger kept at -90 °C through ethanol cooled by an electric

immersion cooler. The software used for performing Ar isotope analysis is "Mass Spec" which is made by Dr. Alan Deino in Berkeley Geochronology Center, USA. Each analysis involves 10 min for gas extraction and purification and 20 min for data acquisition by 8 cycles of peak jumping from mass 40 to mass 36. CO_2 continuous laser was used for the total fusion analyses of the sanidine age standard and K and Ca salts, while the UV pulsed laser was used for analysing the unknown samples. System blanks were measured after every 3 sample analyses. The isotopic ratios of the analysed samples are obtained after the corrections of blank measurements (procedural blanks), mass discrimination by analysis of standard air Ar (atmospheric Ar), interference of the Ar isotopes derived from Ca and K by the neutron irradiation and the decay of the radiogenic Ar isotopes (^{37}Ar and ^{39}Ar) produced by the neutron irradiation.

The sample site spots were ablated by the UV pulse laser with a beam size of 30–50 micron for white mica, 60 sec pulsing duration and a repetition rate of 10 Hz. The number of spots for each single analysis has been set on 5, in order to obtain the necessary amount of sample gas for the enough precision of obtained ages. It was assumed that the incision of the sample by laser do not exceed 100 μm by this condition due to the previously conducted test to examine the depths of produced craters within white micas. In the cases of the fine-grained investigated sites (few tens of microns in size), they may also contain portions of different foliation generations. Furthermore, such areas may not be considered as exclusively constituted of white mica where particularly quartz, chlorite and some matrix material may also be ablated during gas extraction.

5.2 Results

In VS17 sample (**Figure 5a**), for the white mica arranged along S1 foliation, were obtained apparent ages scattered between 41.6 ± 0.6 and 47.2 ± 0.8 Ma, while along S2 foliation obtained apparent ages are scattered between 36.6 ± 0.5 and 37.6 ± 0.6 Ma (**Figure 5b, c, d**). Along S2 main foliation, in fine-grained micro-domains, older apparent ages were also detected (66.5 ± 0.7 Ma and 59.4 ± 0.4 Ma, **Table 2**) due to the presence of other fine-sized K-free minerals (< 20 μm). Consequently, the contribution of non-Wm minerals (e.g., chlorite) provided older ages (see Discussion below), considered not consistent with those obtained on single crystals (or group of homogeneous crystals). The resulting simple average age is 42.6 ± 0.6 (SD = 0.9) Ma for S1, 37.1 ± 0.6 (SD = 0.7) Ma for S2. In addition, in VS17 sample, along a T1-related discrete mylonitic

domains (referred to SM mylonitic foliation), were obtained the apparent age of 39.2 ± 0.4 Ma, as single age (**Figure 5c**).

In VS14 sample (**Figure 5e**), the main foliation (S1) is defined by the preferred orientation of preserved phengite crystal cores, surrounded by S2 muscovite rims (**Figure 5f, g, h**). Along S1 foliation obtained apparent ages are scattered between 42.6 ± 0.9 Ma and 44.9 ± 0.7 Ma in phengite cores, whereas the apparent age of 38.6 ± 0.4 Ma was obtained in muscovite rim (related to S2 foliation development) (**Figure 5f, g, h**). In addition, apparent ages of 32.9 ± 1.8 Ma were obtained with low amount gas emitted during the ablation. In this case, fluids implement a "selective metasomatic overprint", causing local re-crystallization of white mica grains (see Halama et al., 2014). In this case, the amount of emitted gas may lead to obtain younger ages. Because of this, the obtained value should be handled carefully, and considered as a not accurate single age (see **Table 2**).

Along S2 main foliation, in single flakes included in calcite matrix, older apparent ages (54.7 ± 1.4 Ma and 251.5 ± 8.0 Ma, **Figure 5g** and **Table 2**) were also obtained, due to the probable contribution of K-free minerals involved in the laser spot analysis. In addition, in VS14 sample, apparent ages of 39.7 ± 0.8 Ma and 40.6 ± 0.5 were obtained along T1-related discrete mylonitic foliation (SM). The resulting simple average age is 43.7 ± 0.7 Ma (SD = 1.1) for S1 and 40.1 ± 0.7 Ma (SD = 0.6) for SM.

In sample VS15 (**Figure 6a**) the apparent ages that were obtained along the main SM foliation were scattered between 36.3 ± 0.4 Ma and 38.7 ± 0.4 Ma. The analyses measured in micro-lithons on S1 foliation gave apparent ages scattered between of 44.1 ± 0.6 Ma and 46.8 ± 0.4 Ma (**Figure 6b, c, d**). The resulting simple average age is 37.3 ± 0.4 Ma (SD = 1.4) for SM and 45.3 ± 0.5 Ma (SD = 1.0) for S1.

In this sample the fine-grained white mica crystals mixed with chlorite provided some inconsistent results as 63.2 ± 0.6 Ma or 92.3 ± 0.8 Ma (**Figure 6b** and **Table 2**). These analyses gave older ages, because of the low amount of emitted Ar gas from finer K-free chlorite in the ablated spots similarly observed in the above cases (see Discussion below).

The obtained apparent ages for S1 in VS4 (**Figure 6e**) sample are comprised between 40.2 ± 0.5 Ma and 46.4 ± 0.5 Ma (**Figure 6f, g, h**). The resulting simple average age for S1 is 42.9 ± 0.7 Ma (SD = 2.6). The obtained single apparent age on a T1-related kinematic indicator gave 38.8 ± 0.4 Ma.

In VS74 sample (**Figure 7a**), obtained apparent ages on S1 encompasses values between 40.4 ± 0.6 Ma and 46.0 ± 0.6 Ma (**Figure 7b, c, d**), with resulting simple average age of 42.3 ± 0.5 Ma (SD = 1.4). As in previous samples, also in VS74 a few older ages were obtained (53.7 ± 1.8 Ma and 52.9 ± 1.9 Ma) along the same foliation level (see **Figure 7b** and **Table 2**), due to K-free minerals below the surface involved in the ablation. In VS19 sample (**Figure 7e**), obtained apparent ages along S1 micro-lithons are scattered between values of 41.2 ± 0.4 Ma and 43.9 ± 0.4 Ma (**Figure 7f, h**), while along S2 foliation, apparent ages encompass between 37.4 ± 0.4 Ma and 39.7 ± 0.5 Ma (**Figure 7g**). The resulting simple average age is 42.6 ± 0.4 Ma (SD = 1.2) for S1, and 38.8 ± 0.4 Ma (SD = 1.3) for S2. Measured ages along SM foliation gave apparent ages scattered between 38.6 ± 0.3 Ma and 38.9 ± 0.4 Ma (**Figure 7f, g**), for a resulting simple average age of 38.8 ± 0.4 Ma (SD = 0.2). In this sample, the amount of emitted gas was constant, and no older ages were obtained.

6 Discussion

6.1 Significance of individual Age Data

$^{40}Ar/^{39}Ar$ system is classically applied in the context of the "closure temperature" versus "formation temperature" concepts, especially for the case of metamorphic minerals (i.e., white mica). Purdy & Jager (1976) proposed 350°C as the closing T for white mica, based only on certain cooling rate (10°C/m.y.), while T have been lately raised to 500°C (Di Vincenzo et al., 2001; Philippot et al., 2001; Bucher, 2003; Balogh & Dunkl, 2005; Allaz, 2008), based on the assumption that cooling rate is not the only parameter controlling the closure of the white mica.

Several Alpine studies on HP phengites from the axial sector of the belt have shown that the closure temperature is not only the parameter to keep into account for obtained plausible $^{40}Ar/^{39}Ar$ ages (see e.g., Villa, 1998; Di Vincenzo et al., 2001). These studies have emphasized the complexity of the factors controlling argon diffusion. The presence of extraneous ^{40}Ar is due to its incorporation as result of several processes. It may be of external origin by diffusion through grain boundaries (excess argon) or, alternatively by the presence of inherited argon (*in situ* decay), due to re-crystallization. In any case, ages affected by the presence of extraneous ^{40}Ar inevitably leads to obtain older ages, with no geological significance. Nevertheless, Villa et al. (2014), accordingly with Agard et al. (2002), stated in their works that HP phengite normally records

386 formation and/or deformation ages, rejecting the hypothesis of the presence of inherited Ar at the scale of the
387 whole orogen.
388 Villa et al. (2014) and Villa (2015) also stated that, in deformed and sheared rocks, microstructures and
389 chemical composition of the white mica are more important than thermally activated diffusion, which is always
390 slower than other forming processes such as fluid-induced recrystallization and deformation-induced
391 recrystallization (Cole et al., 1983; Lasaga, 1986; Villa, 1998, 2006, 2010; Allaz et al., 2011; Villa & Williams,
392 2013: Villa et al., 2014; Villa, 2015). Thus, the recorded ages of the white micas were interpreted as formation
393 (i.e. deformation) ages, precisely distinct, on microstructural and petrological constrains reported in this study.
394 The observed outliers values in age were explained by existence of mixed population (Wiederkehr et al, 2009),
395 and therefore rejected. Although there are not a plenty of amounts of obtained geochronological data, the
396 distribution of the apparent ages can be used to discriminate the time during which the foliations develop. This
397 time lapse is precisely limited by microstructural evidence and chemical zonation, confirming that iso-
398 orientated white micas, showing the same composition, grew in the time during which the related tectono-
399 metamorphic event occurred.
400
401 **6.2 Structural framework of calculated ages**
402 The combination of microstructural and petrological approaches allowed us to date the different tectonic
403 structures precisely, as long as obtained ages are consistent through the different sampled lithologies
404 (micaschist and calcschist) belonging to the same tectonic unit.
405 The probability diagrams for each sample are summarized in **Figure 8**, showing the maximum probability of
406 ages for each foliation. In these diagrams the obtained ages are shown without outlier data (i.e. data affected
407 by low gas amount or contaminated by ablation of other K-poor phases).
408 Samples from the IPZ (**Figure 8a, b, c**) show two main ages distribution: (i) an older group, with apparent
409 ages scattered between 41.8 ± 0.4 and 46.8 ± 0.4 Ma (blue bars), defined by phengite (S1), and (ii) a younger
410 group, with apparent ages scattered between 36.3 ± 0.4 and 40.6 ± 0.5 Ma (orange bars), representing SM
411 foliation and itself defined by phengite. In samples VS17 and VS14, there is another group of apparent ages,
412 which are scattered between 36.6 ± 0.5 and 38.6 ± 0.4 Ma (green bars), defined by muscovite and attributed to
413 the S2 foliation.

414 Samples from the EPZ (**Figure 8d, e, f**) show a main distribution of values, with apparent ages scattered
415 between 40.2 ± 0.5 and 46.4 ± 0.5 Ma (pale blue bars), and defined by phengite (S1). Other two groups of
416 apparent ages occur in VS19 sample: the first shows values scattered between 38.6 ± 0.4 and 39.0 ± 0.4 Ma
417 (orange bars), defined by phengite and referred to SM foliation, while the second group shows values scattered
418 between 37.4 ± 0.4 and 39.7 ± 0.5 Ma (light green bars), defined by muscovite and attributed to the S2 foliation.
419 A single value referred to SM foliation was measured in sample VS4, giving apparent age of 38.8 ± 0.4 Ma.
420 Along S2 foliation, it was difficult to obtain meaningful and consistent isotopic ages. Indeed, it mainly consists
421 of re-oriented phengite grains, developed during the D1 deformation phase, and of tiny rims of muscovite
422 growing around phengite. Values measured along S2 foliations therefore come from few coarse-grained
423 muscovite grains.
424 The results of absolute chronology are remarkably consistent with the related tectono-metamorphic evolution
425 previously established on macro- meso- and micro observations (Ghignone et al., 2020a; 2020b; 2020c). S1-
426 related phengite grains are older than the other white mica generations, in both IPZ (44.1 ± 0.6 Ma) and EPZ
427 (42.1 ± 0.5 Ma). S2-related muscovite grains are younger than S1-related phengite and show similar apparent
428 ages in both IPZ (37.4 ± 0.4 Ma) and EPZ (37.7 ± 0.4 Ma). SM-related phengite shows a homogeneous group
429 of values (38.0 ± 0.5 Ma), almost coeval with the S2-related muscovite. S1-related phengites, in both IPZ and
430 EPZ, grew during a long-lived tectonic phase (**Figure 9a, d**), which is referred to the first and the second HP
431 metamorphic events (D1), respectively. S2-related muscovite grew during a subsequent second stage (D2),
432 which was coeval to greenschist-facies re-equilibration and exhumation at shallower crustal levels of the
433 tectonic units (**Figure 9b, e**).
434
435 **6. 3 Tectono-metamorphic ages in Western Alpine meta-ophiolite units**
436 The obtained ages can be compared with other data from meta-ophiolite units of the Western Alps whose
437 different tectono-metamorphic stages have been dated.
438 In different units of the IPZ the eclogite-facies stage (D1 of this work) was dated at 49 and 45 Ma in the
439 Monviso meta-ophiolite Complex (Duchene et al., 1997; Rubatto & Hermann, 2003), 51–42 Ma south of the
440 study area (Colle delle Finestre, Agard et al., 2002), 48-44 Ma in the Rocciavrè unit (Angiboust & Glodny,

2020), 48-47 Ma north of the study area (Entrelor, Villa et al., 2014) and 46-42 Ma in the Zermatt-Saas unit (Dal Piaz et al., 2001; Barnicoat et al., 1995; De Meyer et al., 2014; Dragovic et al., 2020).

In EPZ, blueschist-facies stage (D1 of this work) was dated at 45-39 Ma north of the study area (Entrelor; Bucher et al., 2003; Villa et al., 2014) and at 41-36 Ma in the Combin unit (Gouzu et al., 2016).

In both IPZ and EPZ, greenschist stage (D2 in this work) were dated at 42-37 in the Zermatt-Saas unit (Amato et al., 1999; De Meyer et al., 2014; Gouzu et al., 2016), and at 38–35 Ma (Agard et al., 2002) and 40-39 Ma (Villa et al., 2014) south and north of the study area, respectively,.

The shearing event (T1 of this work), responsible for the coupling between IPZ and EPZ, was dated at 37-35 Ma across the Monviso/Rocciavrè and Queyras units (Angiboust & Glodny, 2020), 36-34 Ma (Freeman et al., 1997; Malusà et al., 2005) and 41-34 Ma (Rosenbaum et al., 2012) across the ophiolite units of the Southern Aosta Valley (Entrelor Shear Zone). Coupling between the Zermatt-Saas and Combin units has been dated at 39-37 Ma (Gressoney Shear Zone, Reddy et al., 1999), and 42-37 Ma (Täschalp Shear Zone, Barnicoat et al., 1995; Cartwright & Barnicoat, 2002).

As stated before, the UHP Lago di Cignana Unit were dated at ~ 48 – 40 Ma (Skora et al., 2015; Dal Piaz et al., 2001; Rubatto et al., 1998; Amato et al., 1999; Gouzu et al., 2016), but such metamorphic conditions are conditions not representative for the regional evolution of the Western Alps.

These literature data are overall similar to the ages presented here, highlighting that, in both IPZ and EPZ, the HP event (D1 of this work) occurred during the Middle Eocene (Rosenbaum & Lister, 2005). Our data clearly show the subsequent and regionally less documented greenschist-facies re-equilibration (D2 of this work), developed during the Late Eocene, which is essentially also the age of shearing and tectonic juxtaposition between IPZ and EPZ.

The exhumation history of IPZ and EPZ continued during late deformation phases (D3 and D4, not dated in this work). D3 phase has been dated at around 35-37 Ma in the Queyras units (Agard et al., 2002). Dating of D4 phase and coeval westward T2 shearing along the Susa Shear Zone can be given by considering that they developed at shallow crustal levels and in the field of ductile/brittle transition (see Ghignone et al., 2020b), and therefore consistent with zircon fission-track thermochronological data. Published data (Bernet et al., 2001; Schwartz et al., 2007; Perrone et al., 2011) roughly indicate that the different tectonic units (including the underlying DM Massif) cooled below 200-250° C at around 30 Ma.

6.4 Exhumation rates

Linking isotopic ages with well-constrained retrograde metamorphic paths allows us to calculate exhumation rates (Duchêne et al. 1997; Agard et al. 2009). Here exhumation rates are obtained for the IPZ between the D1 (eclogite-facies conditions, Ghignone et al., 2020c) and D2 (greenschist-facies requilibration) phases. P is assumed here as purely lithostatic, an assumption expected to be valid inside nappes and away from major shear zones – in the latter instead the contributions of oriented (over)pressure cannot be actually neglected (see e.g., Bauville & Yamato, 2021).

The conversion from pressure to depth was calculated by assuming an average density for the meta-ophiolitic units of 3 kg/dm^3, according with the lithostratigraphic successions, and the composition of the IPZ, and considering a lithostatic pressure. The resulting is an average gradient of 0.1 GPa = 3km.

In the IPZ, the HP D1 stage occurred at an average P value of 2.3 GPa (Ghignone et al., 2020c), which would correspond to a depth of ~70 km, while D2-related greenschist-facies re-equilibration occurred at an average P of 0.5 GPa (~15 km).

Our $^{40}Ar/^{39}Ar$ geochronological investigations indicates that in the IPZ, the D1 stage took place at 44 Ma, and greenschist-facies metamorphic re-equilibration were dated at 37 Ma (D2 stage). In the IPZ, the P conditions thus changed from 2.3 GPa to 0.5 GPa in about 6-7 Ma. The resulting exhumation rates would roughly correspond to 8 mm/y (8 km/Ma) for the IPZ.

For the EPZ, Agard et al. (2002) and Villa et al. (2014) proposed realistic exhumation rates of 1-2 mm/y (1-2 km/Ma) in the EPZ area (Northern Queyras and Entrelor Area, respectively), although their peak ages are older than those proposed in this work.

The resulting exhumation rates result faster in the lower IPZ and slower in the upper EPZ (with respect to Agard et al., 2002), (**Figure 10**). This confirm that the IPZ and EPZ were exhumed at different velocities (see the different steepness of black and pale blue/red curves in **Figure 10**) during the westward collision-related tectonic transport, giving rise to the relative Top-to-E sense of shear along the T1-related shear zone (see Ghignone et al., 2020b). This latter apparent tectonic movement opposite to the general westward direction of transport is therefore due to a difference in speed between the units.

Calculated exhumation rate for the IPZ is consistent with those proposed in literature for the other Alpine eclogite-bearing meta-ophiolitic units (**Figure 10**). Exhumation rates of the Rocciavrè (Agard et al., 2002), Zermatt-Saas (De Meyer et al., 2014), Monviso and Rocciavrè (Angiboust & Glodny, 2020) units, roughly range between 6 and 10 mm/y).

7 Tectonic implications and conclusions

The above discussed tectono-metamorphic ages and exhumation rates allow us to summarize the exhumation history of EPZ and IPZ.

1) The geochronological data reported in this paper, discussed with literature petrological and structural data allow providing a pressure – temperature – deformation – time (P – T– d – t) evolution of the IPZ and EPZ meta-ophiolite units of the Western Alps (**Figure 11a, b**). The metamorphic peak of the IPZ, developed under eclogitic conditions (P = 21-25 kbar, T = 500-530 ° C, Ghignone et al., 2020c), at 41 - 46 Ma. The blueschist-facies metamorphic peak of the EPZ developed at a very similar age (40 - 46 Ma), although it occurred at pressures of at least 1.0 GPa lower (1.3 – 1.5 GPa, Agard et al., 2002; Plunder et al., 2012).
2) The agreement among metamorphic ages from different meta-ophiolite units of the Western Alpine belt confirm their near-coeval subduction- and exhumation-related evolution, as also suggested by P-T trajectories defined by Agard et al. (2009), Angiboust et al. (2012) and Ghignone et al. (2020c),
3) The D2-related muscovite-bearing foliation (i.e. the S2), in both IPZ and EPZ, developed during exhumation and under greenschist-facies metamorphic conditions, and almost 6-8 Ma later than the metamorphic peaks (Agard et al., 2002; Ghignone et al. 2020c). The juxtaposition of EPZ and IPZ was nearly coeval to the D2 and was driven by the T1-related shear zone (i.e. the phengite-bearing SM foliation). It should be noted that matching between the D2 and T1 phases implies an almost coeval growth of two different generations of white mica, which correspond to a LP muscovite along S2 and a relative HP phengite along SM foliation. This suggests that the SM-related phengite did not grown under regional metamorphic conditions but in a context of localized overpressure, which can be likely developed along the major shear zone (i.e., the Susa Shear Zone) separating IPZ and EPZ.

This localized P increase can be related to strain variation along T1 shear zones, as a result of the relative movements of IPZ and EPZ during exhumation. The relative motion (Top-to-E kinematics) of the two units along the E-dipping shear zone would result after the different exhumation rates, higher in the IPZ and lower in EPZ (**Figure 10** and **Figure 11a**).

4) The high exhumation rates calculated for the IPZ (7–8 mm/yr) cannot be result only from isostatic uplift or erosion, but needs to be driven by extensional tectonic, buoyancy and/or oriented tectonic forces. It is worth to point out the role played by the SSZ in fast exhumation of the IPZ towards shallow crustal levels compared to the relatively slow exhumation of EPZ (1-2 mm/yr, Agard et al., 2002).

5) Finally, we want to emphasize that the tectonic contact separating the IPZ from the underlying Mesozoic cover of the DM massif has been deformed by D2-folds and developed during a late-D1 stage (Gasco et al. 2011; **Figure 11b**). Taking into account the here presented geochronological data, the coupling between DM and IPZ in the study area should have occurred between 44 Ma (D1 phase) and 37 Ma (D2 phase). This implies that, at least in the northern DM, the D1-related P-T peak age should predate the Early Oliogocene age calculated in the southern DM (i.e. in the Brossasco-Isasca Unit; Moniè and Chopin, 1991; Gebauer et al., 1997; Itaya et al., 2017), wherein a complex tectonic stack of continental crust and ophiolitic units occurs (Henry et al., 1993; Groppo et al., 2019; Balestro et al., 2020).

Declaration of Competing Interest

The authors declare that they have no known competing financial interests or personal relationships that could have appeared to influence the work reported in this paper.

Funding

This work was supported by the German Federal Ministry for Education and Research and the Deutsche Forschungsgemeinschaft (Project FE 1527/2-2 to SF), and by Research grants from University of Torino, Ricerca Locale ‘ex 60%’ 2017–2018 (AB, GB, MG and SG).

References

551 Agard, P., Jolivet, L., & Goffe, B. (2001). Tectonometamorphic evolution of the Schistes Lustrés complex:
552 implications for the exhumation of HP and UHP rocks in the western Alps. Bulletin de la Société
553 géologique de France, 172, 617–636.
554 Agard, P., Monie, P., Jolivet, L., Goffe, B. (2002). Exhumation of the Schistes Lustrés complex: in situ laser
555 probe 40Ar/39Ar constraints and implications for the Western Alps. Journal of Metamorphic Geology,
556 20, 6, 599-618.
557 Agard, P., Yamato, P., Jolivet, L., Burov, E. (2009). Exhumation of oceanic blueschist and eclogites in
558 subduction zones: timing and mechanisms. Earth-Science Reviews, 92, 53–79.
559 Agard, P. (2021). Subduction of oceanic lithosphere in the Alps: Selective and archetypal from (slow-
560 spreading) oceans. Earth Sciences Reviews, 103517.
561 Allaz, J. (2008). Metamorphic evolution in the northern central Alps: Linking 39Ar-40Ar dating with
562 thermobarometry, PhD dissertation. University of Bern, 208 pp.
563 Allaz, J., Berger, A., Engi, M., Villa, I. M. (2011). The effects of retrograde reactions and of diffusion on 39Ar-
564 40Ar ages of micas. Journal of Petrology, 52, 691-716.
565 Amato, J.M., Johnson, C.M., Baumgartner, L.P., Beard, B.L. (1999). Rapid exhumation of the Zermatt-Saas
566 ophiolite deduced from high-precision Sm–Nd and Rb–Sr geochronology. Earth and Planetary Science
567 Letters, 171, 425– 438.
568 Angiboust, S., Agard, P., Jolivet, L., & Beyssac, O. (2009). The Zermatt-Saas ophiolite: the largest (60-km
569 wide) and deepest (c. 70-80km) continuous slice of oceanic lithosphere detached from a subduction zone?
570 Terra Nova, 21, 171-180.
571 Angiboust, S., Langdon, R., Agard, P., Waters, D., & Chopin, C. (2012). Eclogitization of the Monviso
572 ophiolite (W. Alps) and implications on subduction dynamics. Journal of Metamorphic Geology, 30, 37-
573 61.
574 Angiboust, S. & Glodny, J. (2020). Exhumation of eclogitic ophiolitic nappes in the W. Alps: New age data
575 and implications for crustal wedge dynamics. Lithos, 356-357, 105374.
576 Balestro, G., Cadoppi, P., Perrone, G., & Tallone, S. (2009). Tectonic evolution along the Col del Lis-Trana
577 Deformation Zone (internal Western Alps). Bollettino della Società Geologica Italiana, 128(2), 331–339.

578 Balestro, G., Lombardo, B., Vaggelli, G., Borghi, A., Festa, A., Gattiglio, M. (2014). Tectonostratigraphy of
579 the northern Monviso Meta-ophiolite Complex (Western Alps). Italian Journal of Geosciences, 133, 409-
580 426.
581 Balestro, G., Festa, A., Dilek, Y., Tartarotti, P. (2015). Pre-Alpine extensional tectonics of a peridotite
582 localized oceanic core complex in the late Jurassic, high-pressure Monviso ophiolite (Western Alps).
583 Episodes, 38, 266–282.
584 Balestro, G., Festa, A., Borghi, A., Castelli, D., Tartarotti P., & Gattiglio M. (2018). Role of Late Jurassic
585 intra-oceanic structural inheritance in the Alpine tectonic evolution of the Monviso meta-ophiolite
586 Complex (Western Alps). Geological Magazine, 155(2), 233-249.
587 Balestro, G., Festa, A., & Dilek, Y. (2019). Structural Architecture of the Western Alpine Ophiolites, and the
588 Jurassic Seafloor Spreading Tectonics of the Alpine Tethys. Journal of the Geological Society, jgs2018–
589 099. doi:10.1144/jgs2018-099
590 Balestro, G., Nosenzo, F., Cadoppi, P., Fioraso, G., Groppo, C., Festa, A. (2020). Geology of the southern
591 Dora-Maira Massif: insights from a sector with mixed ophiolitic and continental rocks (Valmala tectonic
592 unit, Western Alps). Journal of Maps, 16 (2), 736-744.
593 Balogh, K. & Dunkl, I. (2005). Argon and fission track dating of Alpine metamorphism and basement
594 exhumation in the Sopron Mts. (Eastern Alps, Hungary): Thermochronology or mineral growth?
595 Mineralogy and Petrology, 83, 191 – 218.
596 Barnicoat, A.C., Rex, D.C., Guise, P.G., Cliff, R.A. (1995). The timing of and nature of greenschist facies
597 deformation and metamorphism in the upper Pennine Alps. Tectonics, 14, 279– 293.
598 Bauville, A., & Yamato, P. (2021). Pressure-to-depth conversion models for metamorphic rocks: Derivation
599 and applications. Geochemistry, Geophysics, Geosystems, 22, e2020GC009280.
600 https://doi.org/10.1029/2020GC009280
601 Bearth, P. (1967). Die Ophiolithe der Zone von Zermatt-Saas Fee. Beiträge zur Geologischen Karte der
602 Schweiz, Neue Folge. 132, 130 pp.
603 Bernet, M., Zattin, M., Garver, I., Brandon, M.T., Vance, J., 2001. Steady-state exhumation of the European
604 Alps. Geology 29, 35–38.

Bowtell, S.A., Cliff, R.A., & Barnicoat, A. C. (1994). Sm-Nd isotopic evidence on the age of eclogitization in the Zermatt-Saas ophiolite. Journal of Metamorphic Geology, 12, 187–96.

Bucher, S. (2003). The Briançonnais units along the ECORS-CROP transect (Italian-French Alps): Structures, metamorphism and geochronology, PhD dissertation. University of Basel, 169 pp.

Bucher, K., Fazis, Y., De Capitani, C., Grapes, R. (2005). Blueschists, eclogites, and decompression assemblages of the Zermatt–Saas ophiolite: high-pressure metamorphism of subducted Tethys lithosphere. American Mineralogist, 90, 821–835.

Cartwright, I. & Barnicoat, A.C. (2002). Petrology, geochronology, and tectonics of shear zones in the Zermatt–Saas and Combin zones of the Western Alps. Journal of Metamorphic Geology, 20, 263-281.

Cliff, R.A., Barnicoat, A.C., Inger, S., (1998). Early Tertiary eclogite facies metamorphism in the Monviso Ophiolite. Journal of Metamorphic Geology, 16, 447– 455.

Cole, D. R., Ohmoto, H., Lasaga, A. C. (1983). Isotopic exchange in mineral^fluid systems. I. Theoretical evaluation of oxygen isotopic exchange accompanying surface reactions and diffusion. Geochimica et Cosmochimica Acta, 47, 1681-1693.

Cordey, F., Tricart, P., Guillot, S. & Schwartz, S. (2012). Dating the Tethyan Ocean in the Western Alps with radiolarite pebbles from synorogenic Oligocene molasse basins (southeast France). Swiss Journal of Geosciences, 105, 39–48. DOI: 10.1007/s00015-012-0090-8

Coward, M. P. & Dietrich, D. 1989. Alpine tectonics—an overview. In Alpine Tectonics (eds M. P. Coward, D. Dietrich & R. G. Park), pp. 1–29. Geological Society of London, Special Publication no. 45.

Dal Piaz, G. V., Cortiana, G., Del Moro, A., Martin, S., Pennacchioni, G., Tartarotti, P. (2001). Tertiary age and paleostructural inferences of the eclogitic imprint in the Austroalpine outliers and Zermatt-Saas ophiolite, western Alps. International Journal of Earth Sciences, Geologische Rundschau, 90, 668–684.

Dal Piaz, G. V., Bistacchi, A., & Massironi, M. (2003). Geological outline of the Alps. Episodes, 26, 175-180.

De Meyer, C.M.C., Baumgartner, L.P., Beard, B.L., Johnson, C.M. (2014). Rb–Sr ages from phengite inclusions in garnets from high pressure rocks of the Swiss Western Alps. Earth and Planetary Science Letters, 395, 205–216.

De Togni, M., Gattiglio, M., Ghignone, S., & Festa, A. Pre-Alpine tectono-stratigraphic reconstruction of the Jurassic Tethys in the high-pressure Internal Piedmont Zone (Stura di Viù Valley, Western Alps). Minerals, Special Issue "The ophiolites of the Western Alps", Submitted

Di Vincenzo, G., Ghiribelli, B., Giorgetti, G., Palmeri, R. (2001). Evidence of a close link between petrology and isotope records: Constraints from SEM, EMP, TEM and in situ 40Ar-39Ar laser analyses on multiple generations of white micas (Lanterman Range, Antarctica). Earth Planetary Sciences Letters, 192, 389 – 405.

Dragovic, B., Angiboust, S., & Tappa, J. M. (2020). Petrochronological close-up on the thermal structure of a paleo-subduction zone (W. Alps). *Earth and Planetary Science Letters,* 547, 116446.

Duchêne, S., Blichert-Toft, J., Luais, B., Télouk, P., Lardeaux, J.M., Albarède, F. (1997). The Lu-Hf dating of garnets and the ages of the Alpine high-pressure metamorphism. Nature, 387, 586–9.

Ernst, W. & Dal Piaz, G. (1978). Mineral parageneses of eclogitic rocks and related mafic schists of the Piemonte ophiolite nappe, Breuil-St. Jacques area, Italian Western Alps. American Mineralogist, 63, 621–640.

Festa, A., Balestro, G., Dilek, Y. & Tartarotti, P. 2015. A Jurassic oceanic core complex in the high-pressure Monviso ophiolite (western Alps, NW Italy). Lithosphere 7, 646–52.

Freeman, S. R., Inger, S., Butler, R. W. H., & Cliff, R. A. (1997). Dating deformation using Rb-Sr in white mica: Greenschist facies deformation ages from the Entrelor shear zone, Italian Alps. Tectonics, 16, 57–76.

Gasco, I., Gattiglio, M., & Borghi, A. (2011). Lithostratigraphic setting and P–T metamorphic evolution for the Dora Maira Massif along the Piedmont Zone boundary (middle Susa Valley, NW Alps). International Journal of Earth Sciences, 100, 1065–1085.

Gebauer, D., Schertl, H. P., Brix, M., Schreyer, W. (1997). 35 Ma old ultrahigh—pressure metamorphism and evidence for very rapid exhumation in the Dora Maira Massif, Western Alps. Lithos, 41, 5–24.

Ghignone, S. & Gattiglio, M. (2013). Late to post-metamorphic cross-section trough the Piedmont Zone in the lower Susa Valley (Western Alps). Rendiconti OnLine della Società Geologica Italiana, 29, 66-69.

Ghignone, S., Gattiglio, M., Balestro, G., & Borghi, A. (2020a) Geology of the Susa Shear Zone (Susa Valley, Western Alps). *Journal of Maps*, 16(2), 79- 86. https://doi.org/10.1080/17445647.2019.1698473

659 Ghignone, S., Balestro, G., Gattiglio, M., & Borghi, A. (2020b). Structural evolution along the Susa Shear
660 Zone: new insights for the role of a first-order shear zone in the axial sector of the Western Alps. *Swiss*
661 *Journal of Geosciences* http://doi.org/10.1186/s00015-020-00370-6
662 Ghignone, S., Borghi, A., Balestro, G., Castelli, D., Gattiglio, M., & Groppo, C. (2020c). HP-tectono-
663 metamorphic evolution of the Internal Piedmont Zone in Susa Valley (Western Alps): New petrologic
664 insight from garnet+chloritoid –bearing micaschists and Fe-Ti metagabbro. *Journal of Metamorphic*
665 *Geology* http://doi.org/10.1111/jmg.12574
666 Gouzu, C., Yagi, K., Thanh, N.X., Itaya, T., Compagnoni, R. (2016). White mica K–Ar geochronology of HP–
667 UHP units in the Lago di Cignana area, western Alps, Italy: tectonic implications for exhumation. Lithos,
668 248, 109–18.
669 Groppo, C. & Castelli, D. (2010). Prograde P-T evolution of a lawsonite eclogite from the Monviso meta-
670 ophiolite (Western Alps): Dehydration and redox reactions during subduction of oceanic FeTi-oxide
671 gabbro. Journal of Petrology, 51, 2489-2514.
672 Groppo, C., Beltrando, M., Compagnoni, R. (2009). The P-T path of the ultra-high pressure Lago Di Cignana
673 and adjoining high-pressure meta-ophiolitic units: Insights into the evolution of the subducting Tethyan
674 slab. Journal of Metamorphic Geology, 27, 207-231.
675 Groppo, C., Ferrando, S., Gilio, M., Botta, S., Nosenzo, F., Balestro, G., Festa, A. & Rolfo, F. (2019). What's
676 in the sandwich? New P–T constraints for the (U) HP nappe stack of southern Dora-Maira Massif
677 (Western Alps). European Journal of Mineralogy, 31(4), 665–683.
678 Halama, R., Konrad-Schmolke, M., Sudo., M., Marschall, H. R., Wiedenbeck, M. (2014). Effects of fluid–
679 rock interaction on 40Ar/39Ar geochronology in high-pressure rocks (Sesia-Lanzo Zone, Western Alps).
680 Geochimica et Cosmochimica Acta, 126, 475-494.
681 Handy, M.R., Schmid, S.M., Bousquet, R., Kissling, E., Bernoulli, D. (2010). Reconciling plate-tectonic
682 reconstructions of Alpine Tethys with the geological–geophysical record of spreading and subduction in
683 the Alps. Earth Sciences Review, 102, 121–158.
684 Henry, C., Michard, A., & Chopin, C. (1993). Geometry and structural evolution of ultra-high pressure and
685 high pressure rocks from the Dora-Maira massif, Western Alps, Italy. Journal of Structural Geology,
686 15(8), 965–981. https://doi.org/10.1016/0191-8141(93)90170-F

687 Ishizuka, O. (1998). Vertical and horizontal variations of the fast neutron flux in a single irradiation capsule
688 and their significance in the laser-heating 40Ar/39Ar analysis: Case study for the hydraulic rabbit facility
689 of the JMTR reactor, Japan, Geochemical Journal, 32, 243 – 252.
690 Itaya, T., Yagi, K., Gouzu, C., Thanh, N.X., Groppo, C. (2017). Preliminary report on the excess argon bearing
691 K-feldspar from metagranite in the Brossasco-Isasca UHP Unit of Dora-Maira Massif, Italy. Journal of
692 Mineralogical and Petrological Sciences, 112 (1), 36-39.
693 Itaya, T., Hyodo, H., Imayama, T., & Groppo, C. (2018). Laser step–heating 40Ar/39Ar analyses of biotites
694 from meta–granites in the UHP Brossasco–Isasca Unit of Dora–Maira Massif, Italy. Journal of
695 Mineralogical and Petrological Sciences, 113(4), 171–180.
696 Kelley, S. P., Arnaud, N.O., Turner, S.P. (1994). High spatial resolution 40Ar/39Ar investigations using an
697 ultra-violet laser probe extraction technique. Geochimica et Cosmochimica Acta, 58, 3519 – 3525.
698 Lagabrielle, Y., Brovarone, A.V., Ildefonse, B. (2015). Fossil oceanic core complexes recognized in the
699 blueschist metaophiolites of Western Alps and Corsica. Earth Sciences Reviews 141, 1–26.
700 Lanphere, M. A. & Baadsgaard, H. (2001). Precise K-Ar, 40Ar/39Ar, Rb-Sr and U/Pb mineral ages from the
701 27.5 Ma Fish Canyon Tuff reference standard, Chemical Geology, 175, 653 – 671.
702 Lasaga, A. C. (1986). Metamorphic reaction rate laws and development of isograds. Mineralogical Magazine,
703 50, 359-373.
704 Leardi, L. & Rossetti, P. (1985). Caratteri geologici e petrografici delle metaofioliti della Val d'Ala (valli di
705 Lanzo, Alpi Graie). Bollettino dell'Associazione Mineraria Subalpina, 22, 421-441.
706 Lemoine, M., & Tricart, P. (1986). Les Schistes lustrés des Alpes occidentales: Approche stratigraphique,
707 structurale et sedimentologique. Eclogae Geologicae Helvetiae, 79, 271–294.
708 Lombardo, B. & Pognante, U. (1982). Tectonic implications in the evolution of the Western Alps ophiolite
709 metagabbros. Ofioliti, 7, 371-394.
710 Lombardo, B., Rubatto, D. & Castelli, D. 2002. Ion microprobe U–Pb dating of zircon from a Monviso
711 metaplagiogranite: implications for the evolution of the Piedmont-Liguria Tethys in the Western Alps.
712 Ofioliti 27, 109–17.

Malusà, M.G., Polino, R., & Martin, S. (2005). The Gran San Bernardo nappe in the Aosta valley (Western Alps): a composite stack of distinct continental crust units. Bulletin de la Societe Geologique de France, 176(5), 417-431.

Maluski, H. & Monié, P. (1988). 40Ar/39Ar laserprobe multidating inside single biotites of a Variscan orthogneiss (Pinet Massif Central, France). Chemical Geology, 73, 245 – 263.

Manatschal, G., & Müntener, O., (2009). A type sequence across an ancient magma-poor ocean–continent transition: the example of the western Alpine Tethys ophiolites. Tectonophysics 473, 4–19.

Massonne H. J. & Schreyer W. (1987). Stability field of the high pressure assemblage talc + phengite and two new phengite barometers. European Journal of Mineralogy, 1, 391-410.

Michard, A., Avigad, D., Goff´e, B., Chopin, C., 2004. The high-pressure metamorphic front of the South Western Alps (Ubaye-Maira transect, France, Italy). Schweiz. Mineral. Petrogr. Mitt. 84, 215–235.

Monié, P. & Philippot, P. (1989). Mise en évidence de l'âge éocène moyen du métamorphisme de haute-pression dans la nappe ophiolitique du Monviso (Alpes occidentales) par la méthode 39Ar-40Ar. Comptes rendus de l'Académie des sciences. Série 2, Mécanique, Physique, Chimie, Sciences de l'univers, Sciences de la Terre, 309(2), 245–51.

Monie, P., Chopin, C., 1991. 40Ar/39Ar dating in coesite-bearing and associated units of the Dora Maira massif, Western Alps. Eur. J. Mineral. 239–262.

Negro, F., Bousquet, R., Vils, F., Pellet, C.-M., Hänggi-Schaub, J. (2013). Thermal structure and metamorphic evolution of the Piemont-Ligurian metasediments in the northern Western Alps. Swiss Journal of Geosciences, 106, 63-78.

Nicolas, A. (1966). Étude pétrochimique des Roches vertes et de leurs minéraux entre Dora Maira et Grand Paradis (Alpes piémontaises); le complexe ophiolite-schistes lustrés. PhD dissertation, University of Nantes, France, 299 pp.

Passchier, C.W. & Trouw, R.A.J. (2005). Microtectonics. 2nd edn. Springer, Berlin.

Perrone, G., Eva, E., Solarino, S., Cadoppi, P., Balestro, G., Fioraso, G., et al. (2010). Seismotectonic investigations in the inner Cottian Alps (Italian Western Alps): An integrated approach. Tectonophysics, 496(1–4), 1–16.

740 Perrone, G., Cadoppi, P., Tallone, S., & Balestro, G. (2011). Post-collisional tectonics in the Northern Cottian
741 Alps (Italian Western Alps). International Journal of Earth Sciences, 100(6), 1349–1373.
742 doi:10.1007/s00531-010-0534-1
743 Petrakakis K. & Dietrich H. (1985). MINSORT: A program for processing and archivation of microprobe
744 analyses of silicate and oxide minerals. Neues Jahrbuch fur Mineralogie, Monatshefte, 1985, 379-384.
745 Philippot, P., Blichert-Toft, J., Perchuk, A., Costa, S., Gerasimov, V. (2001). Lu-Hf and Ar-Ar chronometry
746 supports extreme rate of subduction zone metamorphism deduced from geospeedometry, Tectonophysics,
747 342, 23 – 38.
748 Plunder, A., Agard, P., Dubacq, B., Chopin, C., & Bellanger, M. (2012). How continuous and precise is the
749 record of P-T paths? Insights from combined thermobarometry and thermodynamic modelling into
750 subduction dynamics (Schistes Lustrés, W. Alps). Journal of Metamorphic Geology, 30(3), 323–346.
751 Pognante, U. (1979). The orsiera-rocciavrè metaophiolitic complex (Italian Western Alps). Ofioliti, 4, 183-
752 198.
753 Pognante, U. (1980). Preliminary data on the Piemonte ophiolite nappe in the lower Val Susa-Val Chisone
754 area, Italian Western Alps. Ofioliti, 5, 221–240.
755 Polino, R., Dal Piaz, G.V., and Gosso, G., 1990, Tectonic erosion at the Adria margin and accretionary
756 processes for the Cretaceous orogeny of the Alps: Mémoires de la Societé Géologique de France, v. 156,
757 p. 345–367.
758 Purdy, J. W., & Jäger, E. (1976). K-Ar ages on rock forming minerals from the Central Alps. Memorie degli
759 Istituti di Geologia e Mineralogia dell'Universita di Padova, 30, 1 – 32.
760 Reddy, S.M., Wheeler, J., Cliff, R.A. (1999). The geometry and timing of orogenic extension: an example
761 from the Western Italian Alps. Journal of Metamorphic Geology, 17, 573–589.
762 Reddy, S.M., Wheeler, J., Butler, R.W.H., Cliff, R.A., Freeman, S., Inger, S., Pickles, C., & Kelley, S.P.
763 (2003). Kinematic reworking and exhumation within the convergent Alpine Orogen. Tectonophysics.
764 365(1-4), 77-102.
765 Ricou, L.E. & Siddans, W.B. (1986). Collision tectonics in the western Alps. In M. P. Coward & A. C. Ries
766 (Ed.) Collision Tectonics (pp. 229–44). Geological Society of London, Special Publication, 19.

Rosenbaum, G. & Lister, G.S. (2005). The Western Alps from the Jurassic to Oligocene: spatio-temporal constraints and evolutionary reconstructions. Earth Science Reviews, 69, 281–306.

Rosenbaum, G., Menegon, L., Glodny, J., Vasconcelos, P., Ring, U., Massironi, M., Thiede, D., & Nasipuri, P. (2012). Dating deformation in the Gran Paradiso Massif (NW Italian Alps): implications for the exhumation of high-pressure rocks in a collisional belt. Lithos, 144–145, 130–144.

Rubatto, D. & Hermann, J. (2003). Zircon formation during fluid circulation in eclogites (Monviso, Western Alps): implications for Zr and Hf budget in subduction zones. Geochimica et Cosmochimica Acta, 67, 2173–2187.

Rubatto, D., Gebauer, D., Fanning, M. (1998). Jurassic formation and Eocene subduction of the Zermatt-Saas-Fee ophiolites; implications for the geodynamic evolution of the Central and Western Alps. Contributions to Mineralogy and Petrology, 132, 269–287.

Schmid, S.M., Kissling, E., Diehl, T., van Hinsbergen, D.J.J., Molli, G. (2017). Ivrea mantle wedge, arc of the Western Alps, and kinematic evolution of the Alps–Apennines orogenic system. *Swiss Journal of Geosciences,* 110, 581-612.

Schwartz, S., Lardeaux, J.M., Tricart, P., Guillot, S., Labrin, E., 2007. Diachronous exhumation of HP–LT metamorphic rocks from south-western Alps: evidence from fission track analysis. Terra Nova 19 (2), 133–140.

Schwartz, S., Guillot, S., Reynard, B., Lafay, R., Debret, B., Nicollet, C., Lanari, P., Auzende, A.L., 2013. Pressure–temperature estimates of the lizardite/antigorite transition in high pressure serpentinites. Lithos 178, 197–210.

Skora, S., Mahlen, N. J., Johnson, C.M., Baumgartner, L. P., Lapen, T. J., Beard, B.L., Szilvagyi, E.T. (2015). Evidence for protracted prograde metamorphism followed by rapid exhumation of the Zermatt-Saas Fee ophiolite. Journal of Metamorphic Geology, 33, 711–34.

Tartarotti, P., Festa, A., Benciolini, L., & Balestro, G. (2017). Record of Jurassic mass transport processes through the orogenic cycle: Understanding chaotic rock units in the high pressure Zermatt-Saas ophiolite (Western Alps). Lithosphere, 9(3), 399-407.

Tartarotti, P.; Guerini, S.; Rotondo, F.; Festa, A.; Balestro, G.; Bebout, G.; Cannaò, E.; Epstein, G.; Scambelluri, M. (2019). Superposed sedimentary and tectonic block-in-matrix fabrics in a subducted serpentinite mélange (High-Pressure Zermatt Saas Ophiolite, Western Alps). Geosciences 2019, 9, 358.

Tricart, P., Lemoine, M., 1991. The Queyras ophiolite West of Monte Viso (Western Alps): indicator of a pecular ocean floor in the Mesozoic Tethys. J. Geodyn. 13, 163–181.

Uto, K., O. Ishizuka, A. Matsumoto, H. Kamioka, and S. Togashi (1997). Laser-heating 40Ar/39Ar dating system of the Geological Survey of Japan: System outline and preliminary results. Bulletin of the Geological Survey of Japan, 48, 23 – 46.

Villa, I. M. (1998). Isotopic closure. Terra Nova, 10, 42-47.

Villa, I. M. (2006). From the nm to the Mm: isotopes, atomic-scale processes, and continent-scale tectonic models. Lithos, 87, 155-173.

Villa, I. M. (2010). Disequilibrium textures vs equilibrium modelling: geochronology at the crossroads. In: Spalla, M. I., Marotta, A. M., Gosso, G. (eds) Advances in Interpretation of Geological Processes. Geological Society, London, Special Publications 332, 1-15.

Villa, I. M. (2015). 39Ar-40Ar geochronology of mono- and polymetamorphic basement rocks. Periodico di Mineralogia, 84, 3B (Special Issue), 615-632.

Villa, I. M. & Williams, M. L. (2013). Geochronology of metasomatic events. In: Harlov, D. E. & Austrheim, H. (eds) Metasomatism and the Chemical Transformation of Rock. Berlin: Springer, pp. 171-202.

Villa, I.M., Bucher, S., Bousquet, R., Kleinhanns, I.C., Schmid, S.M. (2014). Dating polygenetic metamorphic assemblages along a transect through the Western Alps. Journal of Petrology, 55, 803–830.

Vissers, R. L. M., Van Hinsbergen, D. J. J., Meijer, P. TH., Piccardo, G. B. (2013). Kinematics of Jurassic ultraslow spreading in the Piemonte Ligurian ocean. Earth and Planetary Science Letters, 380, 138–50.

Weber, S., Sandmann, S., Miladinova, I., Fonseca, R. O. C., Froitzheim, N., Münker, C., Bucher, K. (2015). Dating the initiation of Piemonte-Liguria Ocean subduction: Lu–Hf garnet chronometry of eclogites from the Theodul Glacier Unit (Zermatt-Saas zone, Switzerland). Swiss Journal of Geosciences, 108, 183–199.

Whitney, D. L., & Evans, B. W. (2010). Abbreviations for names of rock-forming minerals. American Mineralogist, 95, 185–187. https://doi.org/10.2138/am.2010.3371

Wiederkehr, M., Sudo, M., Bousquet, R., Berger, A., Schmid, S. M. (2009). Alpine orogenic evolution from subduction to collisional thermal overprint: the 40Ar/39Ar age constraints from the Valaisan Ocean, central Alps. Tectonics 28, TC6009.

Wilke, F. D. H., O'Brien, P. J., Gerdes, A., Timmerman, M. J., Sudo, M., Khan, M. A. (2010). The multistage exhumation history of the Kaghan Valley UHP series, NW Himalaya, Pakistan from U–Pb and 40Ar/39Ar ages. European Journal of Mineralogy, 22, 703–719.

Captions

Figure 1: (a) Simplified tectonic sketch-map of the Western Alps, modified after Balestro et al. (2015). Black box indicates the study area. Susa Shear Zone is reported in red. (b) Simplified geological map of the Susa Valley, modified after Ghignone et al. (2020a). Dora Maira (DM), Internal Piedmont Zone (IPZ), External Piedmont Zone (EPZ: metaophiolites, blue; Ambin Massif (AM). Stars indicate the sampling locations.

Figure 2: Representative microstructures and geometric relationships between different foliations of the studied samples at Plane Polarized Light, PPL: (a) VS17, (b) VS14, (c) VS15, (d) VS4, (e) VS74, (f) VS19. Details in **Table 1** and text.

Figure 3: White mica Si vs Al diagram for the studied samples. Different mica genenration are reported in black (S1), red (S2) and green (SM).

Figure 4: Compositional X-ray map of Al content (expressed as wt%) of a detailed microstructure in the VS17 sample, showing different white mica generations oriented along different foliations.

847 **Figure 5:** BSE images of the analysed samples, showing foliations with different orientation and metamorphic
848 ages for IPZ samples (VS17 and VS14). White circles indicate the position of the spots analyses by laser
849 ablation. Blue arrows indicate S1 foliation orientation, green arrows S2 foliation, orange arrows SM foliation.
850 Apparent ages are reported in the boxes and differently coloured accordingly with each foliation generation.
851 (a) BSE map of the whole analyses performed on VS17 sample, white squares indicates the positions of the
852 details reported in (b), (c), (d). (e) BSE map of the whole analyses performed on VS14 sample, white squares
853 indicates the positions of the details reported in (f), (g), (h).
854
855 **Figure 6:** BSE images of the analysed samples, showing foliations with different orientation and metamorphic
856 ages for SSZ samples (VS15 and VS4). White circles indicate the position of the spots analysis by laser
857 ablation. Blue arrows indicate S1 foliation; pale blue arrows indicate S1 foliation, green arrow S2 foliation in
858 IPZ, orange arrows SM foliation. Apparent ages are reported in the boxes and differently coloured accordingly
859 with each foliation generation. The apparent ages without geological significance are highlightened with red
860 contours (a) BSE map of the whole analyses performed on VS15 sample, white squares indicates the positions
861 of the details reported in (b), (c), (d). e) BSE map of the whole analyses performed on VS4 sample, white
862 squares indicate the positions of the details reported in (f), (g), (h).
863
864 **Figure 7:** BSE images of the analysed samples, showing foliations with different orientation and metamorphic
865 ages for EPZ samples (VS74 and VS19). White circles indicate the position of the spots analyses by laser
866 ablation. Pale blue arrows indicate S1 foliation, pale green arrows S2 foliation, orange arrows SM foliation.
867 Apparent ages are reported in the boxes and differently coloured accordingly with each foliation generation.
868 The apparent ages without geological significance are highlighted with red contours (a) BSE map of the whole
869 analyses performed on VS74 sample, white squares indicates the positions of the details reported in (b), (c),
870 (d). e) BSE map of the whole analyses performed on VS19 sample, white squares indicates the positions of
871 the details reported in (f), (g), (h).
872
873 **Figure 8:** Probability diagrams for the investigated samples. In the first row we reported the samples of the
874 IPZ, (a) VS17 sample, (b) VS14 sample, (c) VS15 sample, while in the second row the samples of the EPZ,

(d) VS74 sample, (e) VS19 sample, (f) VS4 sample. We reported in blue the age range referred to S1 foliations, in green the age referred to S2 foliations, in orange the age range referred to SM mylonitic foliation.

Figure 9: Absolute time for the different generations of white mica. (a) S1 in IPZ; (b) S2 in IPZ; (c) SM in both IPZ and EPZ; (d) S1 in EPZ; (e) S2 in EPZ.

Figure 10: Calculated exhumation rates compared in a pressure vs. time diagram for the IPZ (black line), in the graph with the exhumation rates estimated for other meta-ophiolite units of the Western Alps.

Figure 11: (a) Simplified sketch (modified after Angiboust & Glodny, 2020, Ghignone et al., 2020b, Ghignone et al., 2020c) representing the tectonic evolution of the IPZ and EPZ in absolute time during their exhumation path, and their relationships with adjacent DM unit. Continuous lines on top indicates ages from this work, dashed lines represent the uncertainty (D1, D2 and T1). D3 and D4 ages (dashed lines) were inferred from Schwartz et al. (2007) and Perrone et al., (2010). (b) Age versus P diagram, summarizing different tectono-metamorphic stages in time, between IPZ, EPZ and DM (values from Gasco et al., 2011). Black, grey and blue arrows indicate the evolution of IPZ, EPZ and DM, respectively, from D1 to D2, inside the nappes, away from the SSZ.

Table 1: Main petrological and microstructural features of the samples investigated with *in situ* $^{40}Ar/^{39}Ar$ UV laser probe dating.

Table 2: Full results of White Mica $^{40}Ar/^{39}Ar$ in Situ UV Laser Probe Analysis. Obtained ages are reported with 2σ error.

SUPPORTING INFORMATIONS

Table S1: Representative microprobe chemical analysis for the three selected samples.

Table S2: Full Results of White Mica $^{40}Ar/^{39}Ar$ in situ UV Laser Probe Analysis.

903

Figure 1

Click here to access/download;Figure;Figure 1.jpg

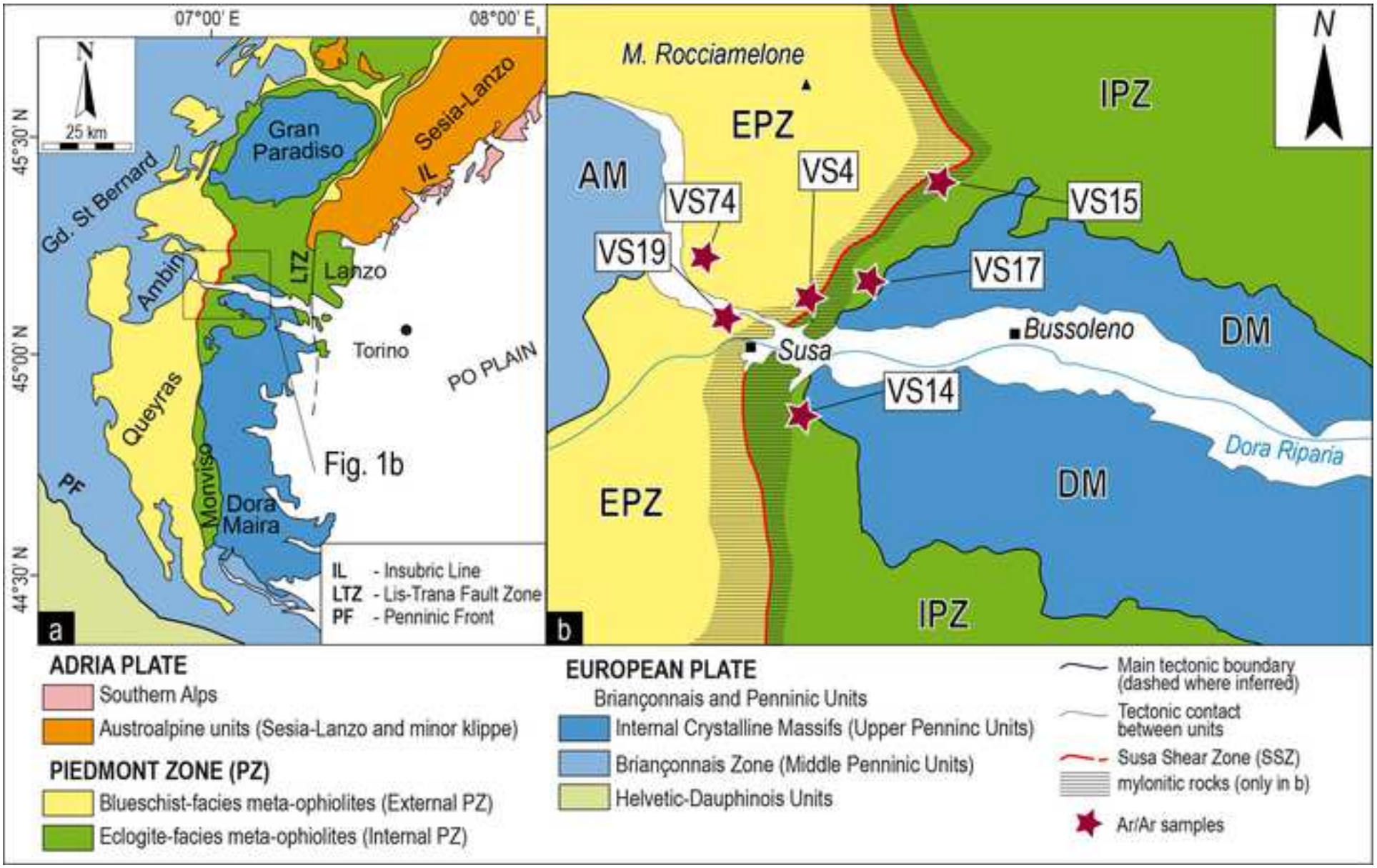

Figure 2

Click here to access/download;Figure;Figure 2.jpg

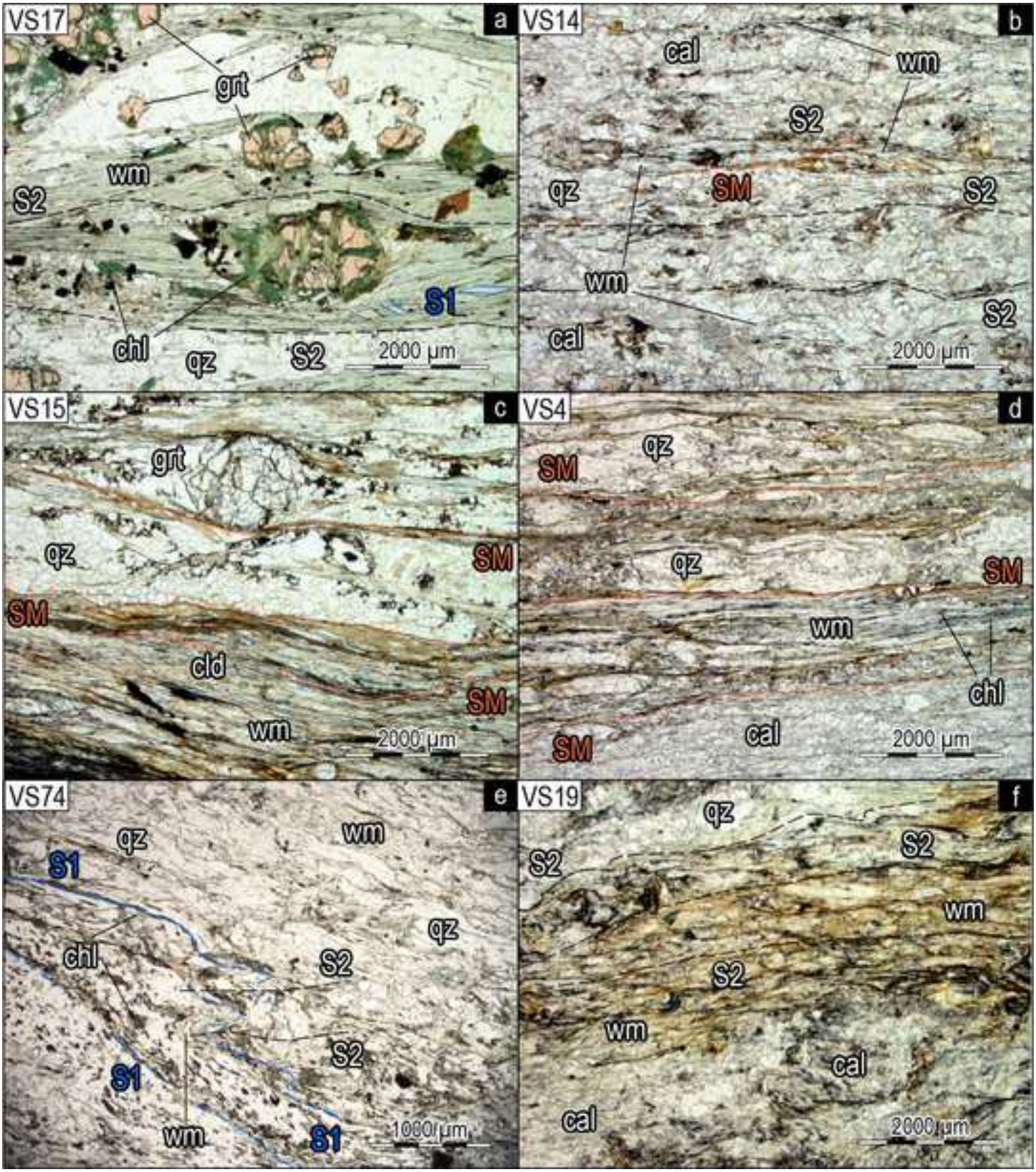

Figure 3

Click here to access/download;Figure;Figure 3.jpg

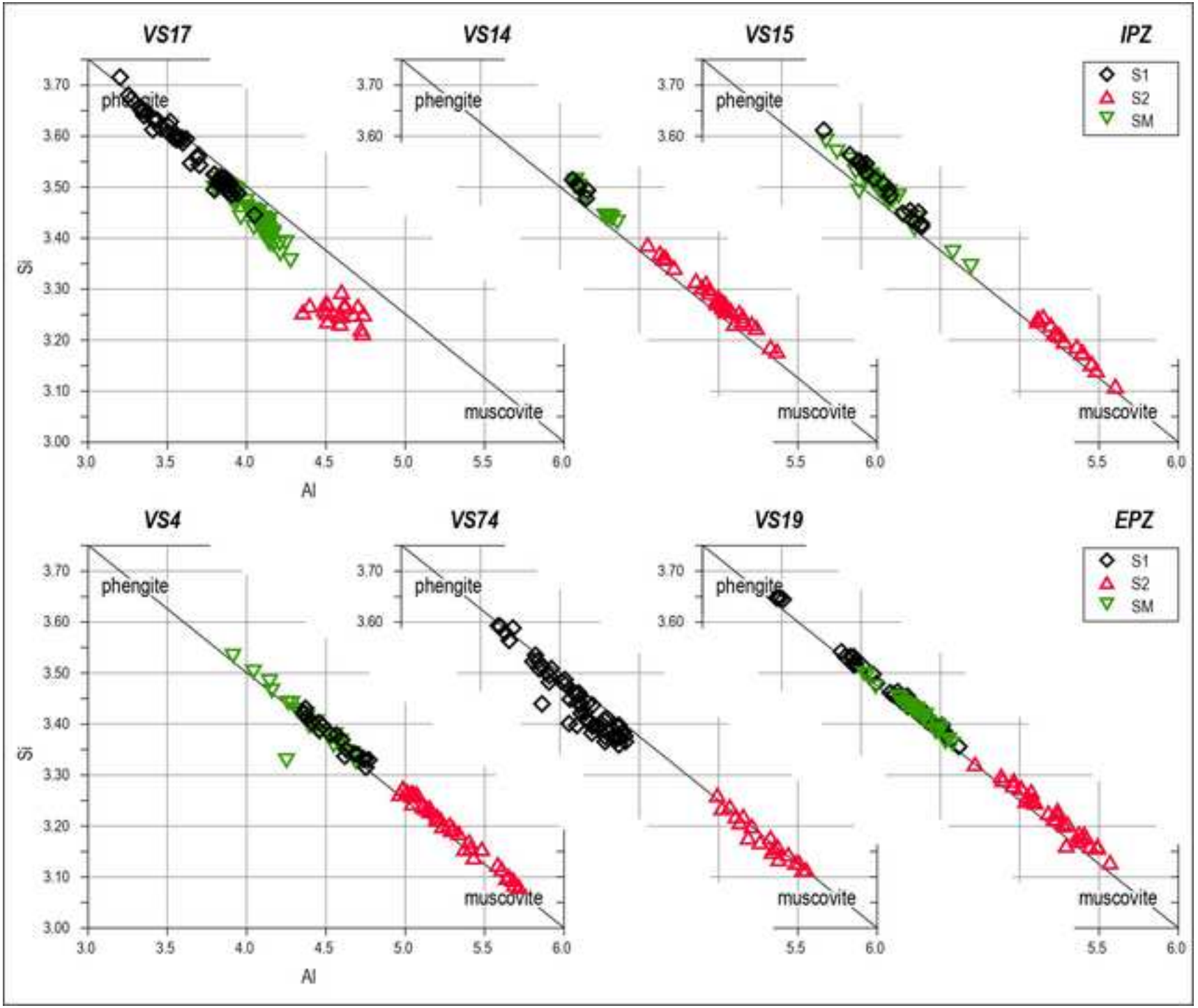

Figure 4

Click here to access/download;Figure;Figure 4.jpg

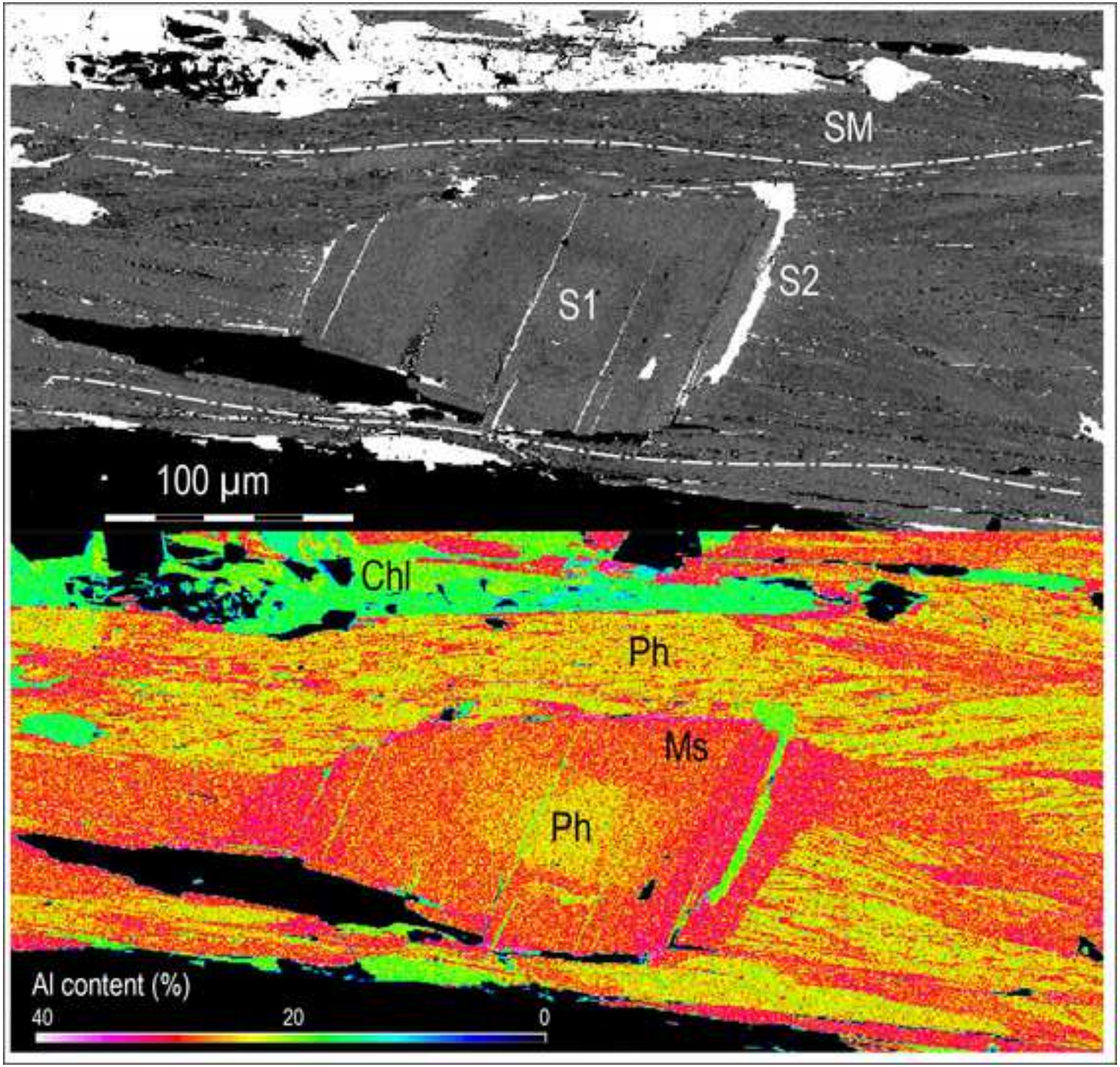

Figure 5

Click here to access/download;Figure;Figure 5.jpg

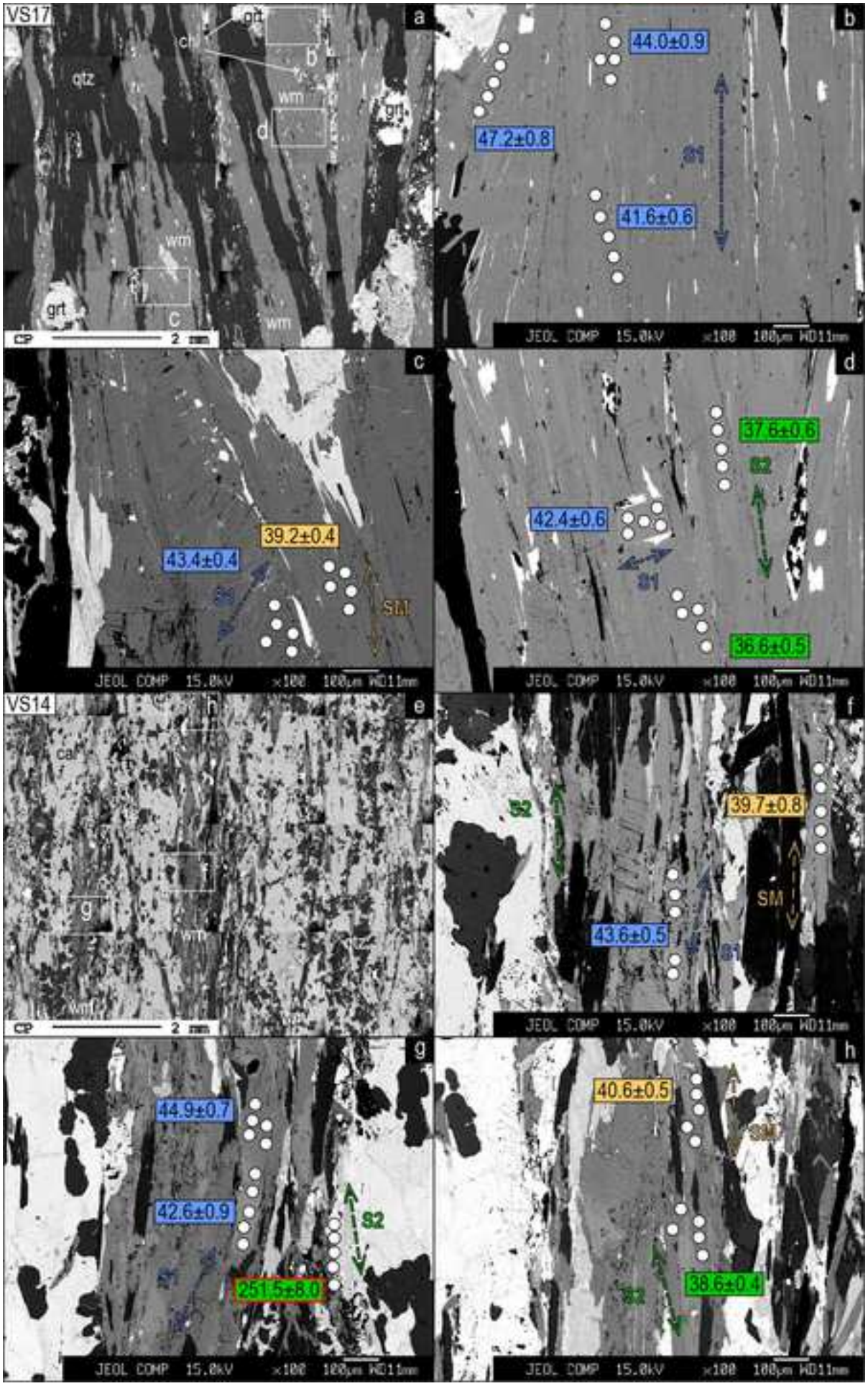

Figure 6

Click here to access/download;Figure;Figure 6.jpg

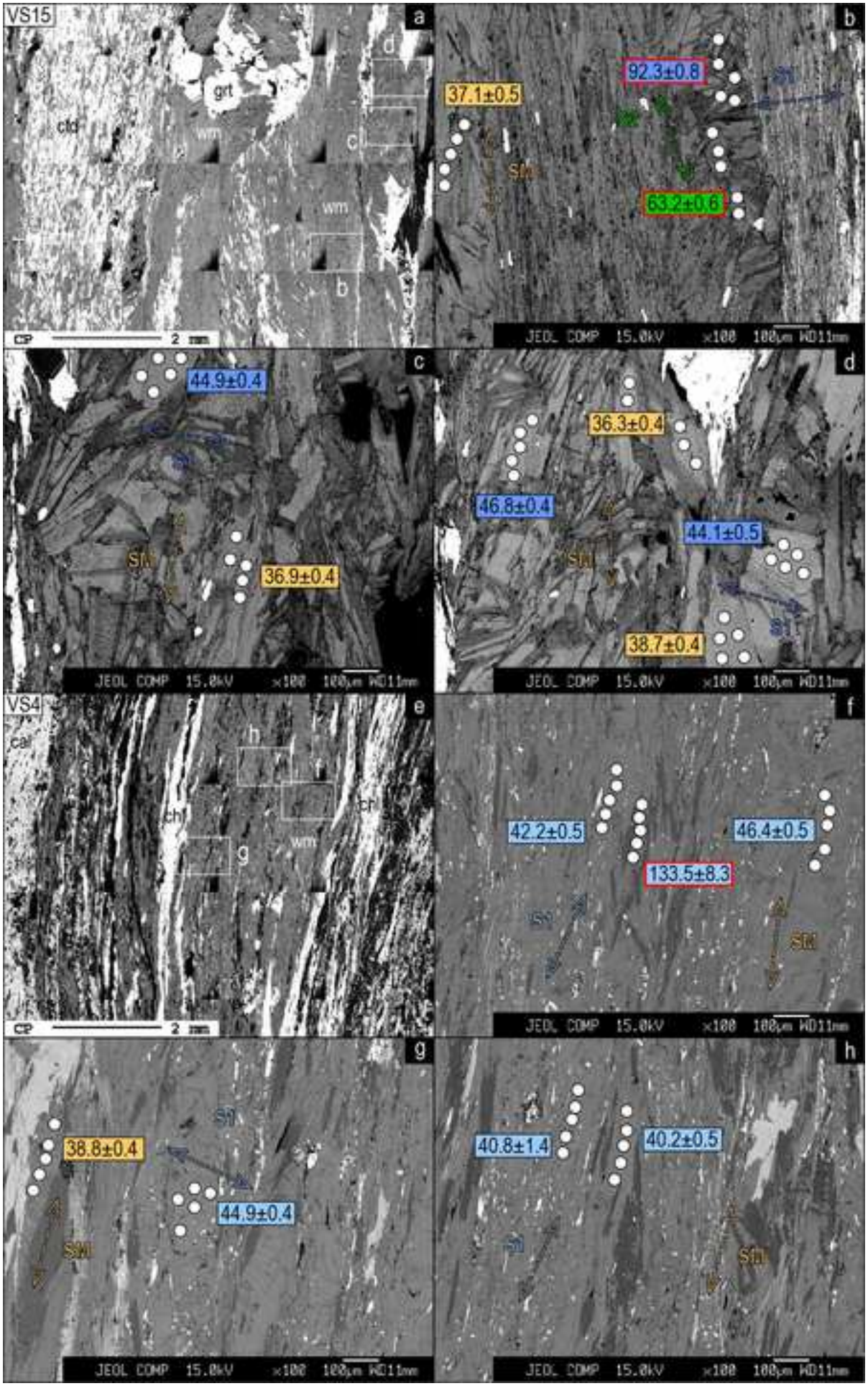

Figure

Click here to access/download;Figure;Figure 7.jpg

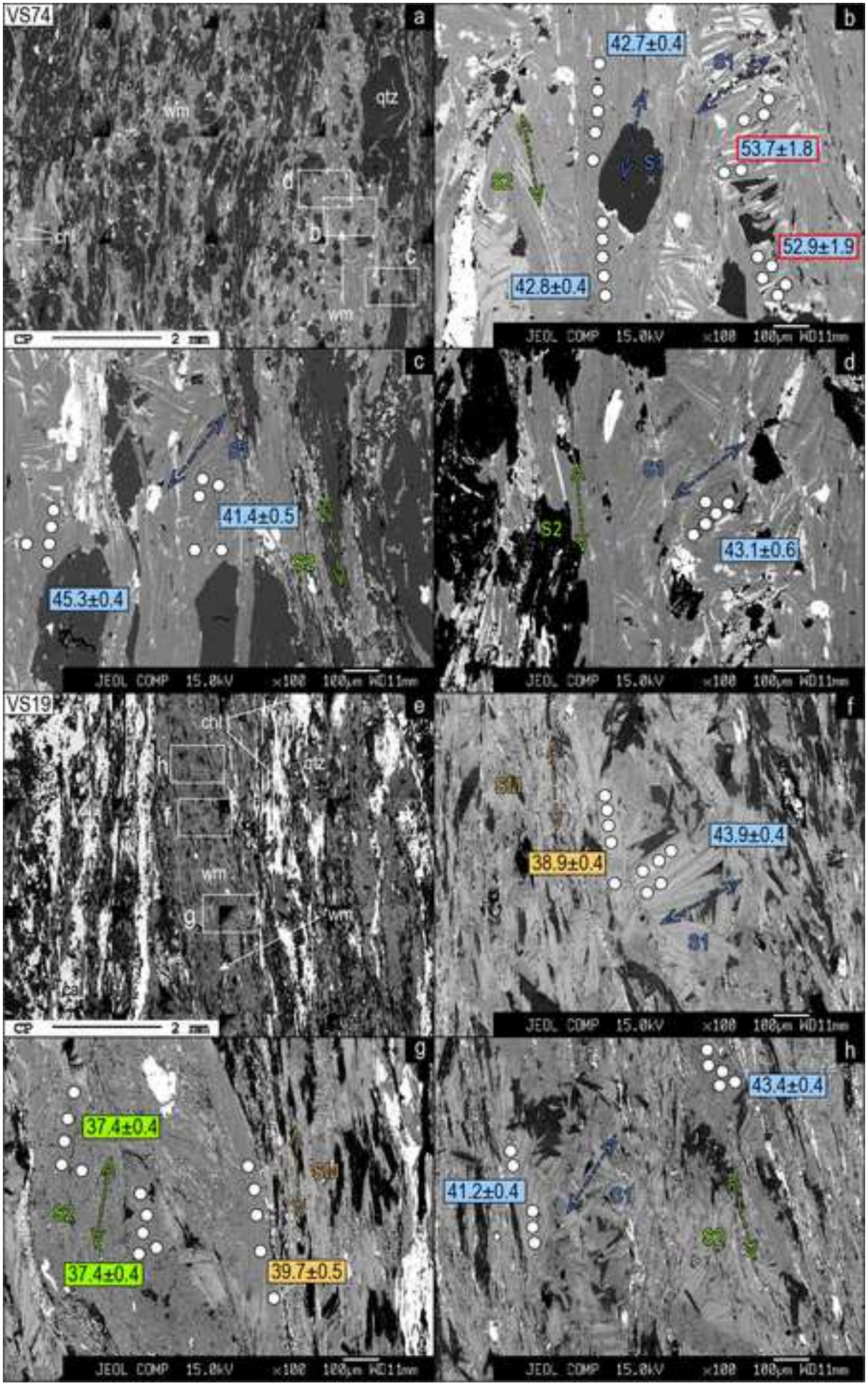

Figure 8

Click here to access/download;Figure;Figure 8.jpg

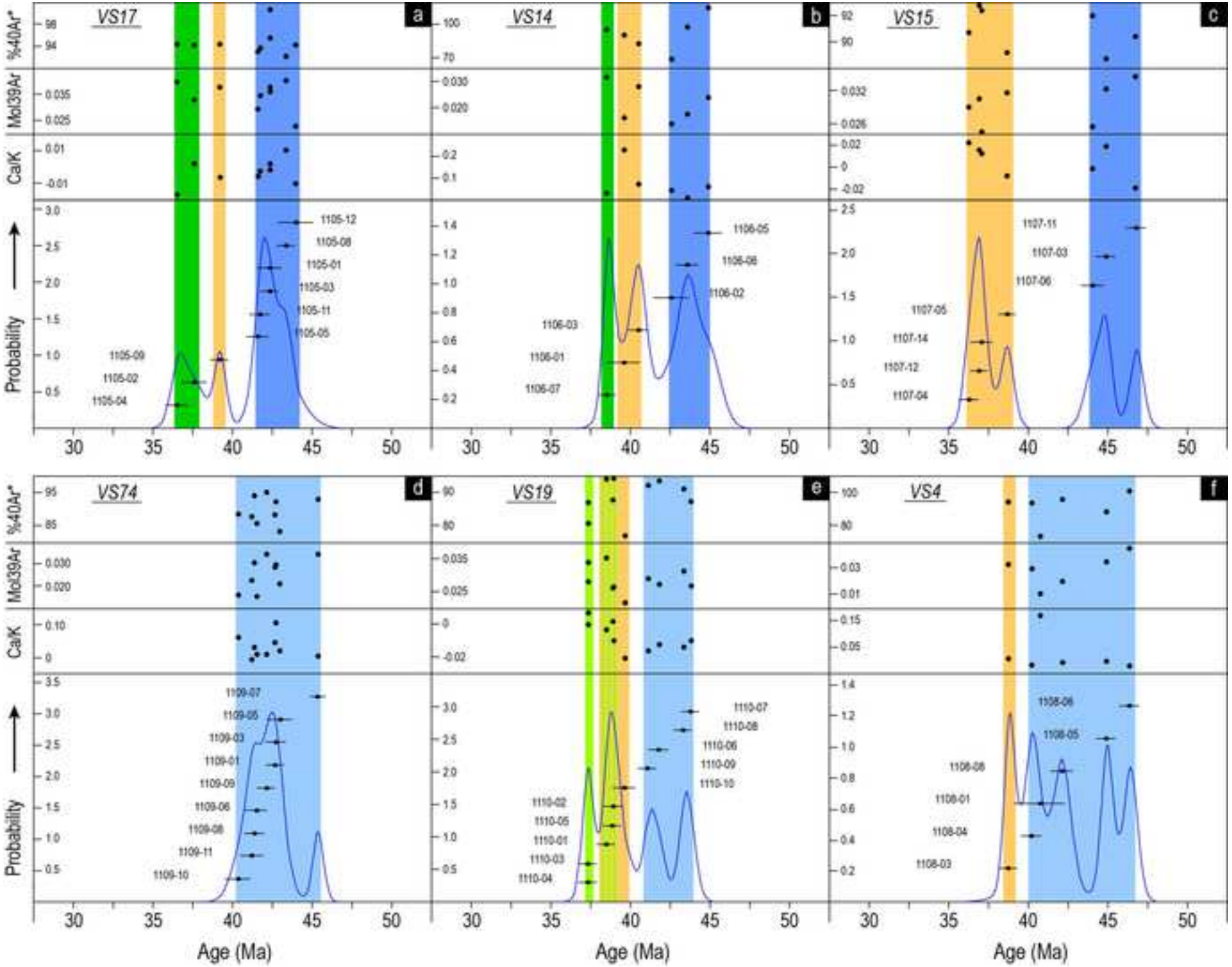

Figure 9

Click here to access/download;Figure;Figure 9.jpg

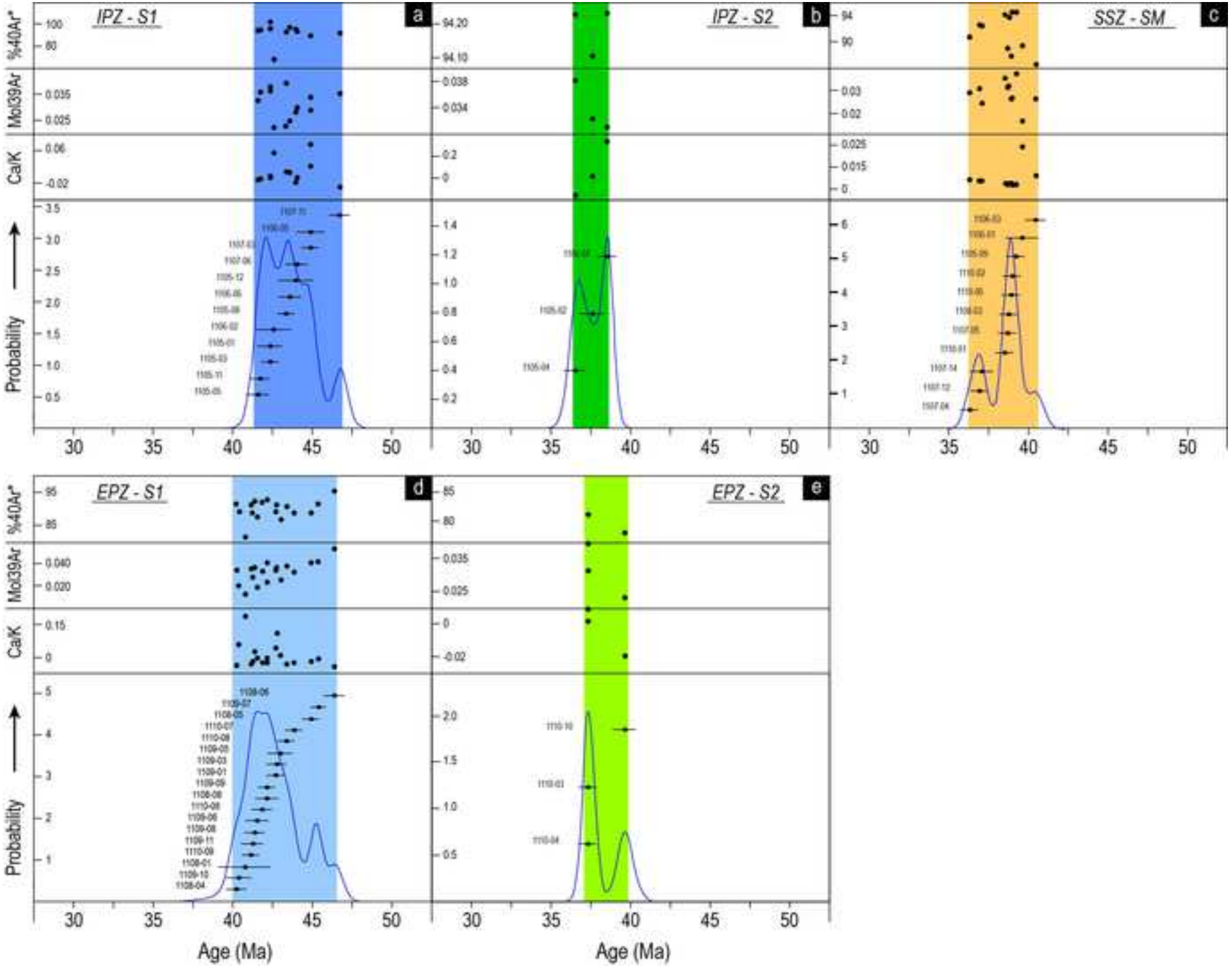

Figure 10

Click here to access/download;Figure;Figure 10.jpg

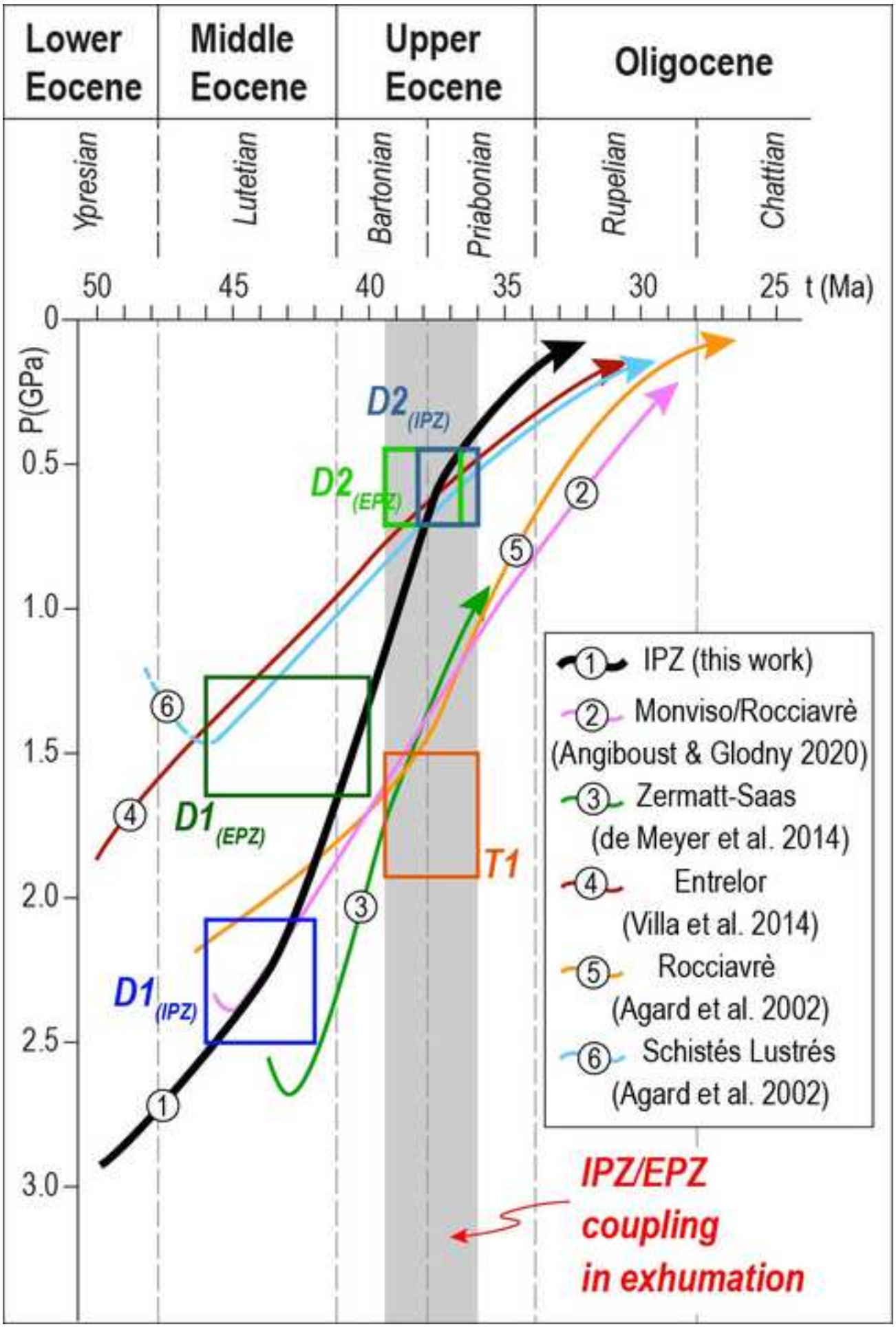

Figure 11

Click here to access/download;Figure;Figure 11.jpg

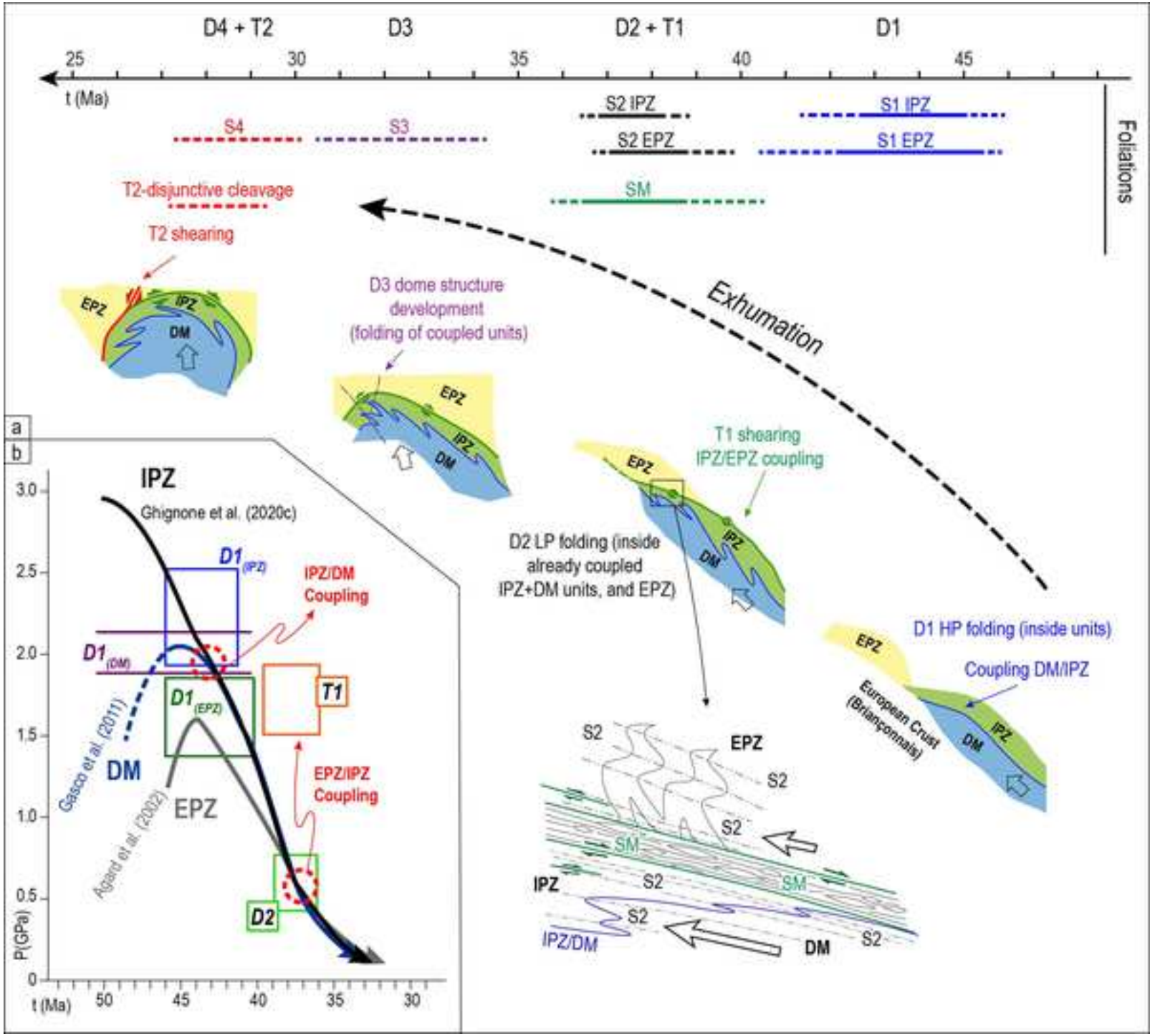

Sample	Lithology	Tectonic domain
VS17	Grt-micaschist	IPZ
VS14	Calcschist	IPZ
VS15	Grt-Cld mylonitic micaschist	IPZ/SSZ
VS4	Mylonitic calcschist	EPZ/SSZ
VS74	Micaschist	EPZ
VS19	Calcschist	EPZ

Mineral assemblage	Foliations	Coordinates
Wm+Qz+Grt+Cld+Chl+Bt (±Pl±Tur)	S1, SM, S2	7°4'45"E 45°8'43"N
Cal+Wm+Qz+Chl	S1, SM, S2	7°3'40"E, 45°7'24"N
Wm+Qz+Grt+Cld+Chl (± Bt)	S1, SM, S2	7°7'10"E, 45°10'28"N
Cal+Wm+Qz+Chl+Bt+Gr	S1, SM, S2	7°4'00"E, 45°8'47"N
Wm+Qz+Chl (± Bt±Pl±Ep)	S1, S2	7°3'31"E, 45°9'5"N
Cal+Wm+Qz+Chl	S1,SM, S2	7°2'27"E 45°8'30"N

Table 2

Run ID	Sample	Tectonic domain	Mineral	Microstructural position	Foliation
1105-01	VS17	IPZ	Ph	Microlithon	S1
1105-02	VS17	IPZ	Ms	Wm rim - main foliation	S2
1105-03	VS17	IPZ	Ph	Wm core - main foliation	S1
1105-04	VS17	IPZ	Ms	Wm rim	S2
1105-05	VS17	IPZ	Ph	Wm core	S1
1105-06	VS17	IPZ	Ms	Wm rim	S2
1105-07	VS17	IPZ	Ph	Microlithon	S1
1105-08	VS17	IPZ	Ph	Wm core	S1
1105-09	VS17	IPZ	Ph	Top-to-E C-plane	SM
1105-10	VS17	IPZ	Ms	Wm rim	S2
1105-11	VS17	IPZ	Ph	Wm core	S1
1105-12	VS17	IPZ	Ph	Wm core	S1
1106-01	VS14	IPZ	Ph	Top-to-E C-plane	SM
1106-02	VS14	IPZ	Ph	Wm core	S1
1106-03	VS14	IPZ	Ph	Top-to-E C-plane	SM
1106-04	VS14	IPZ	Ms	Wm rim	S2
1106-05	VS14	IPZ	Ph	Wm core	S1
1106-06	VS14	IPZ	Ph	Wm core	S1
1106-07	VS14	IPZ	Ms	Wm rim	S2
1106-08	VS14	IPZ	Ms	Wm rim	S2
1106-09	VS14	IPZ	Ms	Wm rim	S2
1107-01	VS15	IPZ/SSZ	Ph	Microlithon (wm core)	S1
1107-02	VS15	IPZ/SSZ	Ph	Microlithon (wm core)	S1

1107-03	VS15	IPZ/SSZ	Ph	Microlithon (wm core)	S1
1107-04	VS15	IPZ/SSZ	Ph	Main (mylonitic) foliation	SM
1107-05	VS15	IPZ/SSZ	Ph	Main (mylonitic) foliation	SM
1107-06	VS15	IPZ/SSZ	Ph	Microlithon (wm core)	S1
1107-07	VS15	IPZ/SSZ	Ph	Microlithon (wm core)	S1
1107-08	VS15	IPZ/SSZ	Ms	Microlithon (wm rim)	S2
1107-09	VS15	IPZ/SSZ	Ph	Main (mylonitic) foliation	SM
1107-10	VS15	IPZ/SSZ	Ms	Microlithon (wm rim)	S2
1107-11	VS15	IPZ/SSZ	Ph	Microlithon (wm core)	S1
1107-12	VS15	IPZ/SSZ	Ph	Top-to-E C-plane	SM
1107-13	VS15	IPZ/SSZ	Ph	Microlithon (wm core)	S1
1107-14	VS15	IPZ/SSZ	Ph	Mylonitic foliation	SM
1108-01	VS4	EPZ/SSZ	Ph	Microlithon	S1
1108-02	VS4	EPZ/SSZ	Ph	Microlithon	S1
1108-03	VS4	EPZ/SSZ	Ph	Main (mylonitic) foliation	SM
1108-04	VS4	EPZ/SSZ	Ph	Microlithon	S1
1108-05	VS4	EPZ/SSZ	Ph	Microlithon	S1
1108-06	VS4	EPZ/SSZ	Ph	Microlithon	S1
1108-07	VS4	EPZ/SSZ	Ph	Main (mylonitic) foliation	SM
1108-08	VS4	EPZ/SSZ	Ph	Microlithon	S1
1108-09	VS4	EPZ/SSZ	Ph	Main (mylonitic) foliation	SM
1108-10	VS4	EPZ/SSZ	Ph	Microlithon	S1
1109-01	VS74	EPZ	Ph	Main foliation (Wmcore)	S1
1109-02	VS74	EPZ	Ph	Qz+chl-rich microlithon	S1

1109-03	VS74	EPZ	Ph	Main foliation (Wm core)	S1
1109-04	VS74	EPZ	Ph	Qz+chl-rich microlithon	S1
1109-05	VS74	EPZ	Ph	Main foliation (Wm core)	S1
1109-06	VS74	EPZ	Ph	Main foliation (Wm core)	S1
1109-07	VS74	EPZ	Ph	Microlithon (Wmcore)	S1
1109-08	VS74	EPZ	Ph	Microlithon (Wm core)	S1
1109-09	VS74	EPZ	Ph	Main foliation (Wm core)	S1
1109-10	VS74	EPZ	Ph	Microlithon (Wm core)	S1
1109-11	VS74	EPZ	Ph	Main foliation (Wm core)	S1
1110-01	VS19	EPZ	Ph	Top-to-E C-plane	SM
1110-02	VS19	EPZ	Ph	Mylonitic foliation	SM
1110-03	VS19	EPZ	Ms	Fine grained main foliation	S2
1110-04	VS19	EPZ	Ms	Fine grained main foliation	S2
1110-05	VS19	EPZ	Ph	Mylonitic foliation	SM
1110-06	VS19	EPZ	Ph	Microlithon (Wm core)	S1
1110-07	VS19	EPZ	Ph	Microlithon (Wm core)	S1
1110-08	VS19	EPZ	Ph	Microlithon (Wm core)	S1
1110-09	VS19	EPZ	Ph	Microlithon (Wm core)	S1
1110-10	VS19	PZ	Ms	Fine grained main foliation	S2

Age±2σ (Ma)	Note
42.4±0.6	
37.6±0.6	
42.4±0.5	
36.6±0.5	
41.6±0.6	
66.5±0.7	Too fine grained
47.2±0.8	K-free phases involved
43.4±0.4	
39.2±0.4	
59.4±0.4	Too fine grained
41.8±0.4	
44.0±0.9	
39.7±0.8	
42.6±0.9	
40.6±0.5	
32.9±1.8	Too fine grained
44.9±0.7	
43.6±0.6	
38.6±0.4	
54.7±1.4	Too fine grained
251.5±8.0	Too fine grained
92.3±0.8	K-free phases involved
68.6±0.6	K-free phases involved

44.9±0.4	
36.3±0.4	
38.7±0.4	
44.1±0.5	
48.4±1.4	Too fine grained
63.2±0.6	Too fine grained
75.2±0.9	Too fine grained
62.7±0.5	K-free phases involved
46.8±0.4	
36.9±0.3	
49.4±0.5	Too fine grained
37.1±0.5	
40.8±1.4	
133.5±8.3	K-free phases involved
38.8±0.4	
40.2±0.5	
44.9±0.4	
46.4±0.5	
51.6±0.7	K-free phases involved
42.2±0.5	
47.4±0.5	Too fine grained
48.7±0.4	Too fine grained
42.7±0.4	
53.7±1.8	K-free phases involved

42.8±0.4	
52.9±1.9	K-free phases involved
43.1±0.6	
41.5±0.6	
45.4±0.4	
41.4±0.5	
42.2±0.4	
40.4±0.6	
41.3±0.5	
38.6±0.4	
39.0±0.4	
37.4±0.4	
37.4±0.4	
38.9±0.4	
41.8±0.5	
43.9±0.4	
43.4±0.4	
41.2±0.4	
39.7±0.5	

Table S1

Supplementary material/Appendix (Files for online publication only)

Table S1.xlsx

Table S2

Supplementary material/Appendix (Files for online publication only)

Table S2.xlsx

Declaration of Competing Interest

The authors declare that they have no known competing financial interests or personal relationships